Politecnico di Torino

Dipartimento Energia "Galileo Ferraris"

Master of Science in Energy and Nuclear Engineering

MHD effect on tritium transport in WCLL at breeder unit level

Thesis advisor
Prof. Massimo Zucchetti

Candidate
Ciro Alberghi

Research correlators
Dr. Raffaella Testoni
Eng. Luigi Candido

A.Y. 2018-2019

Contents

List of Figures

List of Tables

Abstract

The Water-Cooled Lithium-Lead (WCLL) is one of the four breeding blanket concepts proposed by Europe for the demonstrating fusion power reactor DEMO. In the WCLL, tritium, required for the D-T fusion reaction, is produced in the electrically conducting lead-lithium that flows inside the blanket. Its velocity field is strongly influenced by the external magnetic field used for plasma confinement due to a magnetohydrodynamic (MHD) effect, and by the temperature field. The non-isothermal condition is due to the presence of the heat flux incident on the first wall, the plasma-facing area of the blanket, and the volumetric heat generation caused by the flux of energetic particles passing though the component. To avoid high temperatures, the WCLL is cooled with water, flowing in EUROFER tubes. The prediction of the velocity profile of Pb-Li and water is required to compute the transport of tritium inside the module, that allows to determine the T inventory and losses.

In the thesis worj, in a first step, the reliability of the developed MHD codes has been checked solving benchmark cases, analytical and experimental, for which solutions are known. Then, the analysis of the WCLL module has been carried out, using the COMSOL multiphysics tool. Fluid dynamics with buoyancies has been solved for a quarter of module, the minimum relevant domain. MHD effects and tritium transport have been introduced in three simplified geometries with increasing complexity. In particular, a straight duct filled with lead-lithium with zero, one and two coolant tubes has been considered. Different tritium transport mechanisms (advection-diffusion of T into the lead-lithium eutectic alloy, transfer of tritium from the liquid interface towards the EUROFER, diffusion of tritium inside the steel, transfer of tritium from the EUROFER towards the coolant, and advection-diffusion of diatomic T into the water) have been included. With this study, it has been possible to evaluate the temperature field, velocity profiles of both lead-lithium and water and the concentration of tritium in the liquid metal, coolant and pipes.

Sommario

Il WCLL (Water-Cooled Lithium-Lead) è uno dei quattro breeding blanket proposti dall'Europa per il reattore a fusione dimostrativo DEMO. Nel WCLL il trizio, richiesto per la reazione di fusione Deuterio-Trizio, è prodotto nel Piombo-Litio circolante all'interno del blanket, che è elettricamente conduttivo. Il suo campo di velocità è fortemente influenzato dal campo magnetico esterno usato per il confinamento del plasma grazie ad un effetto magnetoidrodinamico (MHD), e dal campo di temperatura. La condizione non isoterma è dovuta alla presenza di un flusso termico incidente sul first wall, l'area del blanket che si affaccia sul plasma, e dalla presenza di generazione di calore volumetrica dovuta dal flusso di particelle che attraversa il componente. Per evitare alte temperature, il WCLL è raffreddato ad acqua, circolante in tubi di EUROFER. La determinazione del profilo di velocità del Pb-Li è richiesta per calcolare il trasporto di trizio nel modulo, che permette di definire l'inventario di T e le perdite.

In questo lavoro di tesi, in un primo passo, è stata verificata l'affidabilità dei codici MHD sviluppati, risolvendo casi di benchmark analitici e sperimentali, di cui le soluzioni sono note. Successivamente è stata effettuata l'analisi del WCLL, utilizzando il software COMSOL multiphysics. È stata risolta la fluidodinamica accoppiata con il trasporto di calore per un quarto di modulo, che è il minimo dominio considerabile. Gli effetti di MHD e il trasporto di Trizio sono stati introdotti in tre geometrie simplificate, con complessità crescente. In particolare è stato considerato un condotto rettangolare di PbLi contenente zero, uno e due tubi. Diversi meccanismi di trasporto del T (avvezione-diffusione del T nel Pb-Li, trasferimento del trizio dal liquido all'EUROFER, diffusione del trizio all'interno del metallo, trasferimento del T dall'EUROFER all'acqua refrigerante e avvezione-diffusione del trizio diatomico nell'acqua) sono stati inclusi. Con questo studio è stato possibile valutare il campo di temperatura, i profili di velocità del Piombo-Litio e dell'acqua e la concentrazione del trizio nel metallo liquido, nel refrigerante e nelle strutture.

Introduction

In the Demonstration Fusion Power Reactor (DEMO), the fuel is a high temperature deuterium-tritium plasma. Differently from deuterium, abundant in nature, tritium must be produced within the power plant. The breeding blanket fulfills this task, and different blanket design are proposed by the EUROfusion Consortium. The Water Cooled Lithium Lead (WCLL) is developed by ENEA, where tritium is produced in the liquid PbLi, that flows under the magnetic field used for plasma confinement. This produces a magnetohydrodynamic effect that influences the flow behavior, and as consequece the tritium transport. The prediction of T concentrations in the blanket is of main interest, both to guarantee fuel self-sufficienty and from a safety point of view.

In the first chapter, a brief description of DEMO and its relevance in the development of nuclear fusion reactors is presented. The different concept of breeding blanket are shown, focusing on the WCLL.

The second chapter displays a formal description of the magnetohydrodynamic effect under the low R_m approximation, and significant case study are solved analytically. The effect of non-isothermal conditions is also included, presenting the analytical solution of relevant magnetoconvection problems. The theoretical description of tritium transport applyed to the WCLL is shown, considering all the relevant phenomena that characterize the transport in the different domains and materials of the blanket. Lastly, the solution strategy of the MHD and transport coupling is presented.

In the third chapter, a method for the verification and validation of MHD codes is followed, in order to check the reliability of the developed codes. Three benchmark problems, consisting of different cases, are solved, and the results are compared to known analytical, numerical or experimental solutions. A 2D fully developed MHD flow is analysed, solving Shercliff and Hunt cases using different codes. A 3D MHD flow in a non-uniform magnetic field is solved and compared to experimental results. Lastly, two cases with buoyancy, differentially and uniformly heated duct, are also investigated.

In the last chapter, the results of the WCLL breeding unit analysis are shown. In the first part, the CFD analysis of half the module has been carried out, starting from a convergence study, in order to limit the discretization error and choose the reference mesh. Next, due to the complexity of the WCLL geometry, MHD and tritium transport are introduced in three simplified geometries, consisting in a rectangular PbLi duct with zero, one or two water tubes. The temperature and velocity fields, and tritium losses and inventories are obtained.

Chapter 1

The DEMO project

1.1 DEMO

The Demonstration Fusion Power Reactor (DEMO) is a crucial step towards the commercial use of fusion power. It will exploit the knowledge gained by the International Thermonuclear Experimental Reactor (ITER) experience, another D-T reactor that is currently under construction since 2003 in Cadarache (France). DEMO is under development by the EUROfusion Consortium with EU Horizon 2020 funds, and shall demonstrate:

1. A high availability for fusion power plants [31].
2. The production of hunderds of MW of electrical energy.
3. The solution of physics and technical issues.
4. The economic feasibility of electric power generation from nuclear fusion reactions.
5. Nuclear safety and acceptable environmental impact (low radioactive waste).
6. Tritium self-sufficiency.

The latter requirement is explained by the fact that DEMO must rely on tritium supply from external sources only for the plant start-up, then, it is expected a tritium consumption of about 22 kg of tritium per year, while the current tritium production capacity from CANDU reactors is currently limited to about 20 kg per year globally [1].

The configuration of the main systems of DEMO is presented in Fig. 1.1. In DEMO the burning plasma is confined in the tokamak thanks to a particular configuration of magnetic fields, generated by superconducting magnets. In particular in the figure the central solenoid, the toroidal field (TF) coils and the poloidal field (PF) coils are shown. Inside the vacuum vessel the high heat flux is discharged in the divertor targets, that intersect the scrape-off layer that contains most of the particles that escape the plasma confinement.

The breeding blanket sorrounds most of the plasma surface, and has different functions. It extracts the power from the reactor for energy production, it shields the sensitive components behind it (for example the magnets) from the incoming flux of high energetic particles, and it breeds tritium. This is possible thanks to the following reactions between neutrons and lithium, that is contained in the blanket.

$$\mathrm{n}^1 + \mathrm{Li}^6 \longrightarrow \mathrm{T}^3 + \mathrm{He}^4 \tag{1.1}$$

$$\mathrm{n}^1 + \mathrm{Li}^7 \longrightarrow \mathrm{T}^3 + \mathrm{He}^4 + \mathrm{n}^1 \tag{1.2}$$

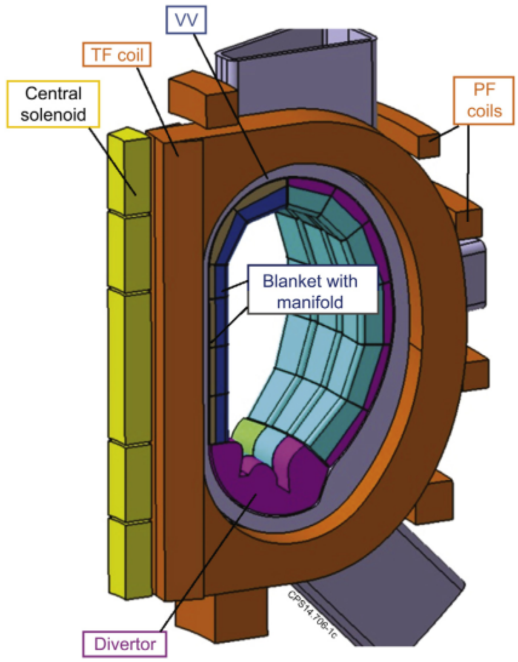

Figure 1.1: Configuration of the DEMO tokamak main systems [2].

The first one has a bigger probability to occur and is exoenergetic, while the latter consumes energy and requires high energy neutrons, but it produces an additional neutron. The tritium breeding ratio (TBR) of a fusion plant is the ratio between the generated and burnt tritium, and must be bigger than one to have tritium self-sufficiency. Looking at the first reaction, that is the more likely, it is evident that the maximum TBR obtainable is 1 and is possible only if every fusion neutron reacts with the Li. To compensate for the neutrons not interacting, and to obtain a TBR bigger than one, the blanket also contains a neutron multiplier, generally beryllium or lead.

Four blanket concepts are currently designed for DEMO reactor. The Helium Cooled Pebble Bed (HCPB) is a solid breeder that uses Li in ceramic form as breeder and beryllium as neutron multiplier. It is researched by KIT, CIEMAT and HAS. The Helium Cooled Lead Lithium (HCLL) uses helium as coolant and eutectic Pb15.8Li as breeder and multiplier, developed by CEA, IPP.CR and KIT. The Dual Coolant Lead Lithium (DCLL) is cooled by PbLi that is also the tritium breeder and multiplier. It works at high temperatures ($> 700°$C) that leads to high thermal efficiency. The last design is the Water Cooled Lead Lithium (WCLL) researched by ENEA and object of this work. It is described in the next section.

1.2 WCLL breeding blanket

The Water Cooled Lead Lithium (WCLL) breeding blanket is cooled by high pressure water and uses eutectic Lead Lithium as neutron multiplier and tritium breeder. The reference design is the WCLL BB 2018 [23]. The DEMO WCLL blanket system is divided into 16 sectors in the toroidal direction, with two inboard and three outboard segmets each. In the poloidal direction the blanket is divided in 7 modules.

The breeding blanket is feeded with water by the manifolds, that develop in poloidal direction, where it enters at 295°C and exits at 328°C, and is connected with the first wall and the breeding zone. The blanket is feeded with PbLi by the PbLi manifolds.

A particular of the outboard segment is presented in Fig. 1.2. Vertical and horizontal stiffening plates reinforce the breeding zone to withstand the thermo-mechanicanical loads for every condition. The

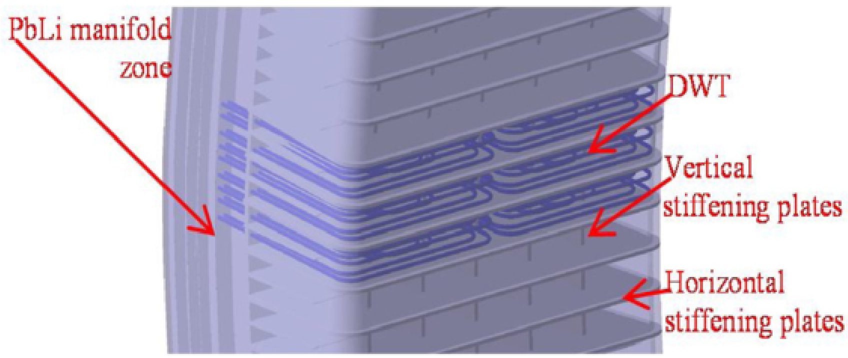

Figure 1.2: WCLL 2018 OB segment [23].

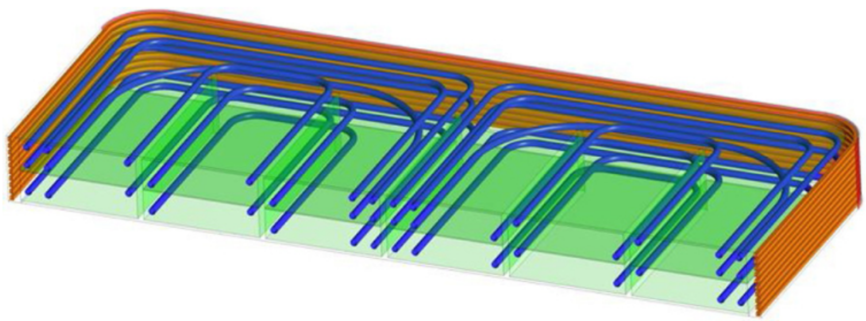

Figure 1.3: WCLL 2018 OB equatorial breeding unit geometry [23].

breeding zone is made by a breeding unit, showed in Figure 1.3 repeated along the poloidal direction. The coolant flows in the double wall tubes (in blue), having inner and outer diameters equal to 8 mm and 13.5 mm respectively, and must ensure a maximum temperature in the structural material, made by Eurofer, below the limit of 550°C. In orange are presented the square coolant channels that removes the heat from the first wall (FW), facing the burning plasma. The FW is coated with a tungsten layer of 2 mm.

The PbLi circulates through the blanket at 328°C and carries the tritium breeded, ultimately to the tritium extraction system. The PbLi is a conducting fluid that flows under the magnetic fields used for plasma confinement, and the resultant magnetohydrodynamic effect lead to an increase in pressure losses, that must be below an acceptable value. In addition, MHD has an impact on the flow behavior, that then affect tritium transport. The distribution of tritium in the breeding blanket is important from a safety point of view, being T a radioactive element, and the losses must be minimized.

Chapter 2

Theoretical background

In the present work, the effect that the presence of a magnetic field has on a liquid metal in motion and finally on the trasport of tritium is analyzed. The equations governing magnetohydrodynamics and tritium transport will be described in this chapter, as well as the introduced assumptions to the development of the investigated problems.

2.1 The magnetohydrodynamic effect

A non magnetic and electrical conducting fluid[1] that flows in presence of a magnetic field is affected and affects $\overline{B}$. This mutual interaction of fluid flow and magnetic fields is what magnetohydrodynamics studies.

The interaction arises as a result of Faraday and Ampere laws and the Lorentz force experienced by a current carrying body. The process can be divided in steps:

1. The relative movement of a conducting fluid and a magnetic field causes an electromotive force thanks to Faraday's law of induction, so electrical currents will develop.

2. Induced currents give rise to an induced magnetic field, according to Ampere's law, that adds to the original magnetic field.

3. The combined magnetic field interacts with the current density giving rise to a Lorentz force that acts on the conductor.

To obtain a mathematical formulation of magnetohydrodynamics, it is necessary to recall the equations that describe the interested physics. In particular, the study of fluid dynamics coupled with electromagnetism requires Navier-Stokes equations of continuity and momentum conservation and the four Maxwell's equations.

Starting from electromagnetism, and, for non magnetic materials, Maxwell's equations are:

$$\nabla \cdot \overline{E} = \frac{\rho_e}{\varepsilon} \tag{2.1}$$

$$\nabla \cdot \overline{B} = 0 \tag{2.2}$$

$$\nabla \times \overline{E} = -\frac{\partial \overline{B}}{\partial t} \tag{2.3}$$

[1]Fluids with these two characteristics are liquid metals, plasmas and strong electrolytes.

$$\nabla \times \overline{B} = \mu \left(\overline{J} + \varepsilon \frac{\partial \overline{E}}{\partial t} \right) \tag{2.4}$$

where $\overline{E}$ and $\overline{B}$ are the electric and magnetic field, $\overline{J}$ is the current density, ρ_e is the charge density, μ is the magnetic permeability and ε is the permittivity. In addition charge conservation 2.5 and Ohm's law 2.6 are considered

$$\nabla \cdot \overline{J} = -\frac{\partial \rho_e}{\partial t} \tag{2.5}$$

$$\overline{J} = \sigma \left(\overline{E} + \overline{u} \times \overline{B} \right) \tag{2.6}$$

where σ is the electric conductivity, $\overline{u}$ is the conductor velocity, and the volumetric Lorentz force

$$\overline{F} = \rho_e \overline{E} + \overline{J} \times \overline{B} \tag{2.7}$$

Considering the purpose of the work, these seven equations may be simplified. Firstly charge density is analyzed. It can be demonstrated that, in conductors that are travelling at speeds much less the speed of light, ρ_e is very small [13]. It follows that the right terms in equations 2.1 and 2.5 are negligible. In addition, $\rho_e \overline{E}$ in Lorentz force equation is really small compared to $\overline{J} \times \overline{B}$. Lastly, in MHD displacement currents are negligible [3], so the Ampere-Maxwell equation 2.4 become Ampere's law. Under these considerations, equations from 2.1 to 2.7 can be rewrtite as follows:

$$\nabla \cdot \overline{B} = 0 \tag{2.8}$$

$$\nabla \times \overline{E} = -\frac{\partial \overline{B}}{\partial t} \tag{2.9}$$

$$\nabla \times \overline{B} = \mu \overline{J} \tag{2.10}$$

$$\nabla \cdot \overline{J} = 0 \tag{2.11}$$

$$\overline{J} = \sigma \left(\overline{E} + \overline{u} \times \overline{B} \right) \tag{2.12}$$

$$\overline{F} = \overline{J} \times \overline{B} \tag{2.13}$$

The equations 2.8 to 2.13 are all that is needed to know about electromagnetism for magnetohydrodynamics.

Now fluid mechanics is considered. Liquid metals can be treated as incompressible fluids, so conservation of mass reduces to continuity equation

$$\nabla \cdot \overline{u} = 0 \tag{2.14}$$

Navier-Stokes equation is:

$$\rho \frac{\partial \overline{u}}{\partial t} + \rho \left(\overline{u} \cdot \nabla \right) \overline{u} = -\nabla p + \mu \nabla^2 \overline{u} + \overline{J} \times \overline{B} \tag{2.15}$$

where we Lorentz force $\overline{J} \times \overline{B}$ is added as an external contribution.

All the equations needed to study MHD have been presented. It is interesting to present four dimensionless numbers which regularly appear in magnetohydrodynamics. The first is the well known Reynolds number

$$Re = \frac{\rho U L}{\mu} \tag{2.16}$$

where L and U are characteristic lenght and velocity scales of the motion. It is representative of the ratio of inertia to viscous forces. The interaction parameter

$$N = \frac{\sigma B^2 L}{\rho U} \tag{2.17}$$

expresses the ratio of the Lorentz force to inertia. The third one is the Hartmann number [15], that represents the ratio of the Lorentz force to viscous forces, and is expressed as

$$Ha = BL\left(\sigma/\mu\right)^{1/2} \tag{2.18}$$

The last dimensionless number is the magnetic Reynolds number

$$R_m = \mu\sigma U L \tag{2.19}$$

that, recalling the transport equation for the magnetic field,

$$\frac{\partial \overline{B}}{\partial t} = \nabla \times \left(\overline{u} \times \overline{B}\right) + \frac{1}{\mu\sigma}\nabla^2 \overline{B} \tag{2.20}$$

is the ratio between the two right members of eq. 2.20. In other words, R_m is the ratio between induction and diffusion of the magnetic field. The magnetic Reynolds number will be now discussed introducing the next assumption, called the low-R_m approximation.

In the present work is studied liquid metal MHD with an imposed steady magnetic field. In this problems the magnitude of u is always kept around $0.001 - 1$ m/s, and considering typical values for σ, μ and l, it follows that R_m<<1 . In this case, the magnetic field associated with induced currents is negligible by comparison with the imposed magnetic field. Simplifications of the governing equations will follow. $\overline{E}_0$, $\overline{B}_0$ and $\overline{J}_0$ are the fields that exist when $\overline{u} = 0$, and $\overline{e}$, $\overline{b}$ and $\overline{j}$ are the infinitesimal perturbations in $\overline{E}$, $\overline{B}$ and $\overline{J}$ which occur due to the presence of a small velocity field. Faraday's law for this quantities became:

$$\nabla \times \overline{E}_0 = 0 \tag{2.21}$$

$$\nabla \times \overline{e} = -\frac{\partial \overline{b}}{\partial t} \tag{2.22}$$

And Ohm's law

$$\overline{J}_0 = \sigma \overline{E}_0 \tag{2.23}$$

$$\overline{j} = \sigma\left(\overline{e} + \overline{u} \times \left(\overline{B_0} + \overline{b}\right)\right) \tag{2.24}$$

In eq. 2.24 the term $\overline{u} \times \overline{b}$ can be neglected being a second order term. Eq. 2.22 gives $\overline{e} \sim u\overline{b}$, so also $\overline{e}$ can be neglected in Ohm's law. Ohm's law for the summed current densities became:

$$\overline{J} = \overline{J}_0 + \overline{j} = \sigma\left(\overline{E}_0 + \overline{u} \times \overline{B_0}\right) \tag{2.25}$$

From 2.21 we know that $\overline{E}_0$ is irrotational, so it is $\overline{E}_0 = -\nabla\phi$, where ϕ is the electric potential. Ohm's law is finally

$$\overline{J} = \sigma\left(-\nabla\phi + \overline{u} \times \overline{B_0}\right) \tag{2.26}$$

and the leading term in the Lorentz force per unit volume is

$$\overline{F} = \overline{J} \times \overline{B}_0 \tag{2.27}$$

The last two equations are all that is required to evaluate Lorentz force.

Summarizing, the following equations describe fully the magnetohydrodynamic effect in the low-R_m approximation for a steady imposed magnetic field $\overline{B}_0$.

$$\nabla \cdot \overline{u} = 0 \tag{2.28}$$

$$\rho \frac{\partial \overline{u}}{\partial t} + \rho \left(\overline{u} \cdot \nabla \right) \overline{u} = -\nabla p + \mu \nabla^2 \overline{u} + \overline{J} \times \overline{B}_0 \tag{2.29}$$

$$\nabla \cdot \overline{J} = 0 \tag{2.30}$$

$$\overline{J} = \sigma \left(-\nabla \phi + \overline{u} \times \overline{B_0} \right) \tag{2.31}$$

In this description of MHD, boundary conditions are still missing. They are presented in the following sections, associated with the respective problems studied.

2.1.1 Shercliff's and Hunt's cases

The laminar, fully developed, incompressible flow of a conducting fluid driven by a pressure gradient along a rectangular duct under an imposed transverse magnetic field is considered. Shercliff [33] and Hunt [16] solved analytically this problem using different boundary conditions. In particular, in Shercliff's case, the four walls of the duct are non-conducting, while in Hunt's case, the two walls perpendicular to the magnetic field are conducting. Hunt's solution will be followed, being Shercliff's the particular case in which the conductivity of the walls is zero.

Considering the assumptions, the time derivative and the intertial term are null in Navier-Stokes equation, and eq. 2.29 becomes

$$0 = -\nabla p + \mu \nabla^2 \overline{u} + \overline{J} \times \overline{B}_0 \tag{2.32}$$

while 2.30 and 2.31 remain the same. Ampere's law is

$$\nabla \times \overline{H} = \overline{J} \tag{2.33}$$

with $\overline{H} = \overline{B}/\mu$ to simplify the notation.

The geometry considered is shown in Figure 2.1.

The flow is directed in z, the imposed magnetic field has an intensity B_0 and is directed in y. Walls AA are parallel to the magnetic field and are called side walls. For the following analysis, they are non-conducting and long $2a$. BB are called Hartmann walls, have a conductivity σ_w and are long $2b$.

Considering that the induced field is small compared to the one imposed, that the only non-null component of $\overline{u}$ is u_z and that conditions, except pressure, are invariant in the z-direction [33], equation 2.31 can be expressed in components as follows:

$$J_x = \sigma \left(-\frac{\partial \phi}{\partial x} - u_z B_0 \right) \tag{2.34}$$

$$J_y = \sigma \left(-\frac{\partial \phi}{\partial y} \right) \tag{2.35}$$

Current conservation and Ampere's law give

$$\frac{\partial J_x}{\partial x} + \frac{\partial J_y}{\partial y} = 0 \tag{2.36}$$

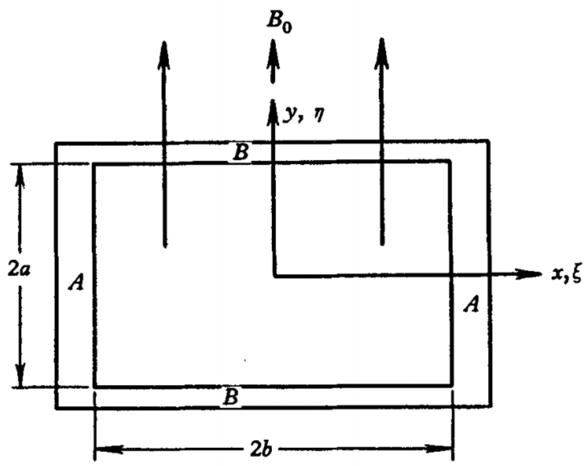

Figure 2.1: Cross-section of the rectangular duct with magnetic field in y-direction. The walls AA lie at $x =^+_- b$ and BB at $y =^+_- a$ [16].

$$J_x = \frac{\partial H_z}{\partial y} \tag{2.37}$$

$$J_y = -\frac{\partial H_z}{\partial x} \tag{2.38}$$

and Navier-Stokes

$$0 = -\frac{\partial p}{\partial z} + \mu \left(\frac{\partial^2}{\partial x^2} + \frac{\partial^2}{\partial y^2} \right) u_z + J_x B_0 \tag{2.39}$$

Now the derivative in y of 2.34 and the derivative in x of 2.35 are obtained:

$$\frac{\partial J_x}{\partial y} = \sigma \left(-\frac{\partial^2 \phi}{\partial x \partial y} - B_0 \frac{\partial u_z}{\partial y} \right) \tag{2.40}$$

$$\frac{\partial J_y}{\partial x} = \sigma \left(-\frac{\partial^2 \phi}{\partial x \partial y} \right) \tag{2.41}$$

Substituting Eq. 2.41 in 2.40

$$\frac{\partial J_x}{\partial y} - \frac{\partial J_y}{\partial x} = -\sigma B_0 \frac{\partial u_z}{\partial y} \tag{2.42}$$

and 2.37, 2.38 in 2.42

$$0 = B_0 \frac{\partial u_z}{\partial y} + \frac{1}{\sigma} \left(\frac{\partial^2}{\partial x^2} + \frac{\partial^2}{\partial y^2} \right) H_z \tag{2.43}$$

Substituting 2.37 and 2.38 in Navier-Stokes equation we get:

$$0 = -\frac{\partial p}{\partial z} + B_0 \frac{\partial H_z}{\partial y} + \mu \left(\frac{\partial^2}{\partial x^2} + \frac{\partial^2}{\partial y^2} \right) u_z \tag{2.44}$$

To simplify the notation $V = u_z\mu/\left(-\frac{\partial p}{\partial z}\right)/a^2$, $H = H_z\mu^{1/2}/\left(-\frac{\partial p}{\partial z}\right)/a^2/\sigma^{1/2}$, and $l = b/a$, $\xi = x/a$, $\eta = y/a$. Being a the characteristic length of this problem, the Hartmann number is $Ha = aB_0(\sigma/\mu)^{1/2}$. Finally, Equations 2.43 and 2.44 become:

$$\frac{\partial^2 H}{\partial \xi^2} + \frac{\partial^2 H}{\partial \eta^2} + Ha\frac{\partial V}{\partial \eta} = 0 \tag{2.45}$$

$$\frac{\partial^2 V}{\partial \xi^2} + \frac{\partial^2 V}{\partial \eta^2} + Ha\frac{\partial H}{\partial \eta} = -1 \tag{2.46}$$

The boundary condition on H for the two conducting walls is the thin wall condition, calling t the wall thickness and n the versor normal to the wall

$$\frac{\partial H}{\partial n} = H\frac{\sigma a}{\sigma_w t} \tag{2.47}$$

valid when $t << a$. We can call $c_w = \frac{\sigma_w t}{\sigma a}$ wall conductivity ratio. The boundary condition on V is the no-slip condition ($V = 0$) at the walls.

Hunt [16] found an analytical solution starting from Equations 2.45 and 2.46, expressing H and V as Fourier series in ξ, with coefficients functions of η,

$$V = \sum_{k=0}^{\infty} v_k(\eta)\cos\alpha_k\xi \tag{2.48}$$

$$H = \sum_{k=0}^{\infty} h_k(\eta)\cos\alpha_k\xi \tag{2.49}$$

$$1 = \sum_{k=0}^{\infty} a_k(\eta)\cos\alpha_k\xi \tag{2.50}$$

where $\alpha_k = (k+1/2)\frac{\pi}{l}$ and $a_k = \frac{2(-1)^k}{\alpha_k l}$. Substituting these in 2.45 and 2.46 we get:

$$v_k'' - \alpha_k^2 v_k + Ha h_k' = -a_k \tag{2.51}$$

$$h_k'' - \alpha_k^2 h_k + Ha v_k' = 0 \tag{2.52}$$

with boundary conditions at $\eta =^+_- 1$, $V = 0$ and $\frac{\partial H}{\partial \eta} =^-_+ H/c_w$, at $\xi =^+_-$, $V = 0$ and $H = 0$. The solution found by Hunt contains hyperbolic functions that, for high Ha, give values out of the range of any existing computer. Ni *et al.* [24] reformulated Hunt's formula as

$$V = \sum_{k=0}^{\infty} \frac{2(-1)^k\cos(\alpha_k\xi)}{l\alpha_k^3}(1 - V2 - V3) \tag{2.53}$$

$$V2 = \frac{\left(c_w r_{2k} + \frac{1-exp(-2r_{2k})}{1+exp(-2r_{2k})}\right)\frac{exp(-r_{1k}(1-\eta))+exp(-r_{1k}(1+\eta))}{2}}{\frac{1+exp(-2r_{1k})}{2}c_w N + \frac{1+exp(-2(r_{1k}+r_{2k}))}{1+exp(-2r_{2k})}} \tag{2.54}$$

$$V3 = \frac{\left(c_w r_{1k} + \frac{1-exp(-2r_{1k})}{1+exp(-2r_{1k})}\right)\frac{exp(-r_{2k}(1-\eta))+exp(-r_{2k}(1+\eta))}{2}}{\frac{1+exp(-2r_{2k})}{2}c_w N + \frac{1+exp(-2(r_{1k}+r_{2k}))}{1+exp(-2r_{1k})}} \tag{2.55}$$

$$H = \sum_{k=0}^{\infty} \frac{2(-1)^k\cos(\alpha_k\xi)}{l\alpha_k^3}(H2 - H3) \tag{2.56}$$

$$H2 = \frac{\left(c_w r_{2k} + \frac{1-exp(-2r_{2k})}{1+exp(-2r_{2k})}\right)\frac{exp(-r_{1k}(1-\eta))+exp(-r_{1k}(1+\eta))}{2}}{\frac{1+exp(-2r_{1k})}{2}c_w N + \frac{1+exp(-2(r_{1k}+r_{2k}))}{1+exp(-2r_{2k})}} \tag{2.57}$$

$$H3 = \frac{\left(c_w r_{1k} + \frac{1-exp(-2r_{1k})}{1+exp(-2r_{1k})}\right)\frac{exp(-r_{2k}(1-\eta))+exp(-r_{2k}(1+\eta))}{2}}{\frac{1+exp(-2r_{2k})}{2}c_w N + \frac{1+exp(-2(r_{1k}+r_{2k}))}{1+exp(-2r_{1k})}} \tag{2.58}$$

where

$$N = \left(Ha^2 + 4\alpha_k^2\right)^{1/2} \tag{2.59}$$

$$r_{1k}, r_{2k} = \frac{1}{2}\left(\pm Ha + N\right) \tag{2.60}$$

and l, c_w and α_k have the already shown expression. The calculated V from eq. 2.53 can therefore be used to calculate u_z, from the definition of V

$$u_z = \mu^{-1} V \left(-\frac{\partial p}{\partial z}\right) a^2 \tag{2.61}$$

and the current densities J_x and J_y can be found from Ampere's law (equations 2.37 and 2.38) including the definition of H found in eq. 2.56

$$J_x = \mu^{-1/2}\frac{\partial H}{\partial y}\left(\frac{\partial p}{\partial z}\right) a^2 \sigma^{1/2} \tag{2.62}$$

$$J_y = \mu^{-1/2}\frac{\partial H}{\partial x}\left(\frac{\partial p}{\partial z}\right) a^2 \sigma^{1/2} \tag{2.63}$$

where $\frac{\partial H}{\partial y}$ and $\frac{\partial H}{\partial x}$ are

$$\frac{\partial H}{\partial y} = \sum_{k=0}^{\infty} \frac{2(-1)^k \cos(\alpha_k \xi)}{l\alpha_k^3}\left(\frac{\partial H2}{\partial y} - \frac{\partial H3}{\partial y}\right) \tag{2.64}$$

$$\frac{\partial H2}{\partial y} = \frac{\left(c_w r_{2k} + \frac{1-\exp(-2r_{2k})}{1+\exp(-2r_{2k})}\right)\frac{\frac{r_{1k}}{a}\exp(-r_{1k}(1-\eta))+\frac{r_{1k}}{a}\exp(-r_{1k}(1+\eta))}{2}}{\frac{1+\exp(-2r_{1k})}{2}c_w N + \frac{1+\exp(-2(r_{1k}+r_{2k}))}{1+\exp(-2r_{2k})}} \tag{2.65}$$

$$\frac{\partial H3}{\partial y} = \frac{\left(c_w r_{1k} + \frac{1-\exp(-2r_{1k})}{1+\exp(-2r_{1k})}\right)\frac{\frac{r_{2k}}{a}\exp(-r_{2k}(1-\eta))+\frac{r_{2k}}{a}\exp(-r_{2k}(1+\eta))}{2}}{\frac{1+\exp(-2r_{2k})}{2}c_w N + \frac{1+\exp(-2(r_{1k}+r_{2k}))}{1+\exp(-2r_{1k})}} \tag{2.66}$$

$$\frac{\partial H}{\partial x} = \sum_{k=0}^{\infty} \frac{-2(-1)^k \frac{\alpha_k}{a}\sin(\alpha_k \xi)}{l\alpha_k^3}\left(H2 - H3\right) \tag{2.67}$$

Another quantity that will be used is the volumetric flow rate, that can be found, dimensionless, integrating V on the cross section of the duct.

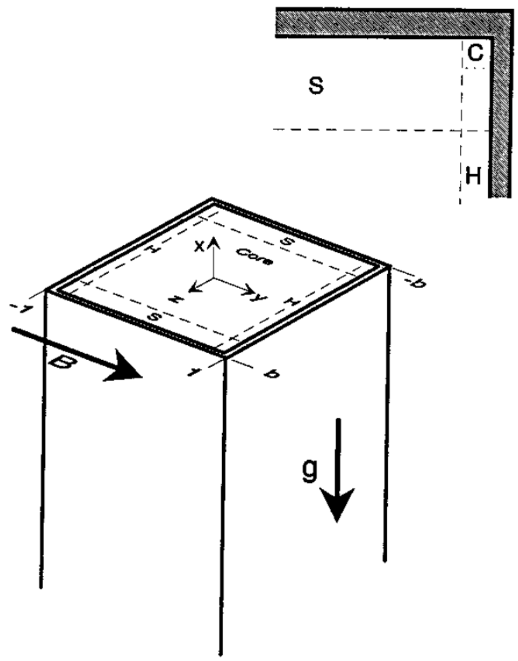

Figure 2.2: Channel geometry. Harmann layers are denoted by “H” and side layers by “S”. “C” are the corner regions [7].

$$
\begin{aligned}
\widetilde{Q} &= \int_{-1}^{1}\left(\int_{-l}^{l} V d\xi\right) d\eta \\
&= \sum_{k=0}^{\infty} \frac{2(-1)^k}{l\alpha_k^4}\left(\sin(\alpha_k l) - \sin(-\alpha_k l)\right) \\
&\left(2 - \frac{c_w r_{2k} + \frac{1-\exp(-2r_{2k})}{1+\exp(-2r_{2k})}}{\frac{1+\exp(-2r_{1k})}{2} c_w N + \frac{1+\exp(-2(r_{1k}+r_{2k}))}{1+\exp(-2r_{2k})}}\left(\frac{1}{r_{1k}} - \frac{1}{r_{1k}}\exp(-2r_{1k})\right)\right. \\
&\qquad \left. - \frac{c_w r_{1k} + \frac{1-\exp(-2r_{1k})}{1+\exp(-2r_{1k})}}{\frac{1+\exp(-2r_{2k})}{2} c_w N + \frac{1+\exp(-2(r_{1k}+r_{2k}))}{1+\exp(-2r_{1k})}}\left(\frac{1}{r_{2k}} - \frac{1}{r_{2k}}\exp(-2r_{2k})\right)\right)
\end{aligned}
\tag{2.68}
$$

and the dimensional volumetric flow rate is

$$
Q = \widetilde{Q}\left(\frac{\partial p}{\partial z}\right) a^4/\mu \tag{2.69}
$$

2.1.2 Magnetoconvection

The flow of the electrically conducting fluid caused by buoyancy in a long vertical channel of rectangular cross section is considered. The imposed magnetic field is $\overline{B} = B_0\widehat{y}$ and the gravitational acceleration $\overline{g} = -g\widehat{x}$ is alligned with the channel axis, as shown in figure 2.2.

In order to consider the buoyancy forces, heat transfer, in addition to magnetohydrodynamics, must be solved. The temperature distribution is governed by

$$\rho c_p \frac{\partial T}{\partial t} + \rho c_p \left(\overline{u} \cdot \nabla\right) T = k \nabla^2 T + Q \tag{2.70}$$

where T is the temperature, ρ is the density of the fluid, c_p is its isobaric specific heat and k is the thermal conductivity and Q is the volumetric heat source. The MHD equations (from eq. 2.28 to 2.31) are still valid, but the gravity term $\rho \overline{g}$ must be added to 2.29. For the stationary case and in dimensionless form, the equations governing magnetoconvection become

$$\nabla \cdot \overline{u} = 0 \tag{2.71}$$

$$\frac{Gr}{Ha^4} \left(\overline{u} \cdot \nabla\right) \overline{u} = -\nabla p + \frac{1}{Ha} \nabla^2 \overline{u} + \overline{J} \times \widehat{y} + T \widehat{x} \tag{2.72}$$

$$\nabla \cdot \overline{J} = 0 \tag{2.73}$$

$$\overline{J} = -\nabla \phi + \overline{u} \times \widehat{y} \tag{2.74}$$

$$Pe \left(\overline{u} \cdot \nabla\right) T = \nabla^2 T + Q \tag{2.75}$$

where $\overline{u}$ and $\overline{J}$ are the velocity and the electric current density vectors, scaled by the reference quantities $u_0 = \rho_0 \beta g \Delta T / \sigma B^2$ and $J_0 = \sigma u_0 B$. T is the difference between the local temperature and the reference temperature T_0, scaled by the characteristic temperature difference ΔT. ρ_0 is the density of the fluid at T_0 and β is the thermal expansion coefficient of the fluid, according to the Boussinesq approximation. The difference between the local pressure and the isothermal hydrostatic pressure at T_0, scaled by $L J_0 B$ is called p, where L is a typical length scale measured in direction of the magnetic field. V is the electric potential scaled by $L u_0 B$ and Q is the volumetric heat source scaled by $k \Delta T / L^2$. Lastly, $Ha = LB(\sigma/\rho_0 \nu)^{1/2}$ is the already known Hartmann number,

$$Gr = \beta g \Delta T L^3 / \nu \tag{2.76}$$

is the Grashof number, that express the importance of buoyant effects,

$$Pe = u_0 L \rho_0 c_p / k \tag{2.77}$$

is the Peclet number that gives the ratio of convective to the conductive heat flux.

The boundary conditions are the no-slip condition at the duct walls,

$$\overline{u} = 0 \tag{2.78}$$

and the thin wall condition for electric currents

$$\overline{J} \cdot \widehat{n} = c_w \nabla_w^2 \phi \tag{2.79}$$

where $\widehat{n}$ is the versor normal to the wall and ∇_w^2 is the two-dimensional Laplacian in the plane of the wall. The thermal conditions are

$$T = T_w \tag{2.80}$$

for a perfectly conducting wall or

$$\widehat{n} \cdot \nabla T = -q_w \tag{2.81}$$

for a given wall heat flux q_w.

It is possible now to introduce some simplifications. Firstly, considering that the fluid has an excellent thermal conductivity, that is fairly valid for liquid metals, Pe<<1, so the convective heat flux is negligible.

The temperature distribution becomes independent of the flow, and can be calculated in a first step. The last simplification is that the interaction parameter $N = \frac{\sigma B^2 l}{\rho u} = Ha^4/Gr$ is sufficiently large. In this case, inertia effects in the momentum balance can be neglected. It is a reasonable assumption, because, for the problems addressed in this work, the value of Ha is generally $10^3 - 10^4$. The simplificated equations are

$$0 = \nabla^2 T + Q \tag{2.82}$$

$$\nabla \cdot \overline{u} = 0 \tag{2.83}$$

$$0 = -\nabla p + \frac{1}{Ha}\nabla^2 \overline{u} + \overline{J} \times \widehat{y} + T\widehat{x} \tag{2.84}$$

$$\nabla \cdot \overline{J} = 0 \tag{2.85}$$

$$\overline{J} = -\nabla \phi + \overline{u} \times \widehat{y} \tag{2.86}$$

with the already discussed boundary conditions.

For high values of Ha the flow region splits into distinct subregions, as shown in figure 2.2. In the core region viscosity effects are negligible, and the momentum is balanced between the pressure gradient ∇p, the Lorentz force $\overline{J} \times \widehat{y}$ and the buoyant force $T\widehat{x}$. Viscosity plays its role within the boundary layers near walls. The viscous layers perpendicular to the magnetic field are called Harmann layers and their thickness scales with Ha^{-1}. The layers parallel to $\overline{B}$ are called side layers, and they scale with $Ha^{-1/2}$. Depending on the wall conductivity ratio c_w, the side layers can carry a significant fraction of the total flow rate.

Buhler [7] solved analytically the problem using matched asymptotic method, taking advantage of the different characteristics of the flow regions. In a first step the core solution is obtained, in a second step the core solution is matched with the solution in the Hartmann layers and, finally, the solution in the side layers is calculated. The corner regions are not considered explicitly since they do not carry a significant flow rate and they match the solution in the side layers with the solution in the Hartmann layers.

A duct closed at both the ends is considered. There is no forced pressure difference applied to generate the flow, that is purely buoyancy driven. The channel is long enough that a fully developed regime establishes within a significantly large region along the channel axis. In these conditions, the total net flow rate in the duct cross section must be zero.

Two applications are considered. In the first problem, a uniform heat flux $\nabla T = \widehat{z}$ crosses the duct between the isothermal walls at $z = ^{+}_{-} b$. The temperature profile is symmetric with respect to $y = 0$ and is simply

$$T = z \tag{2.87}$$

The potential ϕ in the three subregions is:

$$\phi_H = \frac{1}{2} c_H^{-1} z^2 \tag{2.88}$$

$$\phi_{core} = \phi_H + \frac{1}{2}\left(y^2 - 1\right) \tag{2.89}$$

$$\phi_s = \frac{1}{2}\left(y^2 - 1\right)\left(\frac{b}{c_s + 1}\right) \tag{2.90}$$

where c_H and c_s are the wall conductivity ratios for the Hartmann walls near the Hartmann layers and for the side walls near the side layers. The only nonzero velocity component is u_x, and for the core is

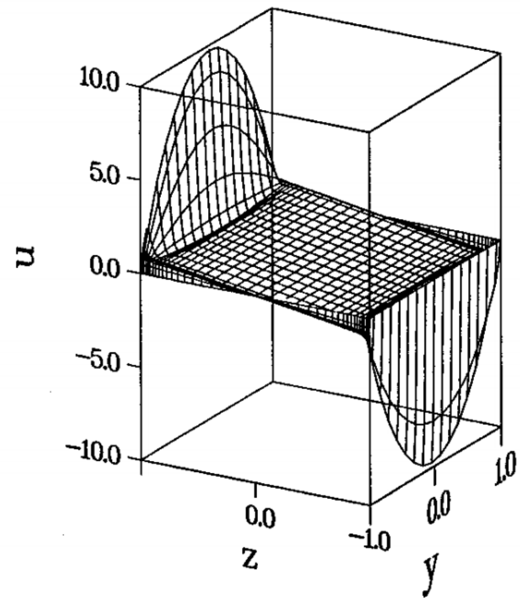

Figure 2.3: Velocity distribution in a perfectly conducting duct with $T = z$ and $Ha = 1000$ [7].

$$u_{x,core} = \left(c_H^{-1} + 1\right) z \tag{2.91}$$

and for the side layer is

$$u_{x,s} =^{+}_{-} 4\frac{\alpha}{\beta^3}\left(\frac{b}{c_s} + 1\right) Ha^{1/2}\exp(-\alpha\zeta)\sin(\alpha\zeta)\cos(\beta y) \tag{2.92}$$

at $z =^{+}_{-} b$, where $\alpha = \pi^{1/2}/2$, $\beta = \pi/2$ and the side layer coordinate $\zeta = Ha^{1/2}(b - z)$. The velocity distribution in the duct for $c_s = c_H = \infty$ and $Ha = 1000$ is shown in figure 2.3.

In the second application a uniform volumetric heat generation across the duct $Q = 1$ is considered. Harmann walls are adiabatic, and the side walls are kept at the same constant temperature. The temperature takes the form

$$T = -\frac{1}{2}z^2 + \Theta \tag{2.93}$$

The core potential is

$$\phi_{core} = \phi_H - \frac{z}{2}\left(y^2 - 1\right) \tag{2.94}$$

with the Harmann potential

$$\phi_H = \frac{z}{c_H}\left(\Theta - \frac{z^2}{6}\right) \tag{2.95}$$

The velocity in the core is

$$u_{x,core} = \frac{1}{2}\left(1 - y^2 - \left(1 + c_H^{-1}\right) z^2\right) + \left(1 + c_H^{-1}\right)\Theta \tag{2.96}$$

and in the side layer is

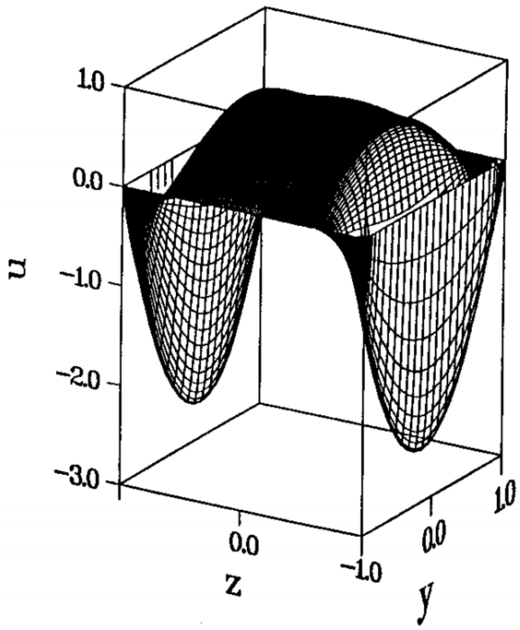

Figure 2.4: Velocity distribution in a perfectly conducting duct with a volumetric heat generation $Q = 1$ and $Ha = 100$ [7].

$$u_{x,s} = -4\frac{\alpha}{\beta^3}\left(b + c_s^{-1}\left(\Theta - \frac{b^2}{2}\right)\right) Ha^{1/2}\exp(-\alpha\zeta)\sin(\alpha\zeta)\cos(\beta y) \tag{2.97}$$

Θ is found from the condition that the total net flow rate must be zero

$$\int_{-1}^{1}\left(\int_{-b}^{b}(u_{x,core} + u_{x,s})\,dz\right)dy = 0 \tag{2.98}$$

and is

$$\Theta = \frac{b^2}{6}\frac{\left(1 + c_H^{-1}\right)b - c_s^{-1}}{\left(1 + c_H^{-1}\right)b - c_s^{-1}/3} \tag{2.99}$$

The velocity profile for a perfectly conducting duct and $Ha = 100$ can be seen in fig. 2.4.

2.2 Tritium transport in the WCLL-BB of DEMO

Tritium is produced within the liquid PbLi due to the following reactions between neutrons and lithium:

$$\mathrm{n}^1 + \mathrm{Li}^6 \longrightarrow \mathrm{T}^3 + \mathrm{He}^4 \tag{2.100}$$

$$\mathrm{n}^1 + \mathrm{Li}^7 \longrightarrow \mathrm{T}^3 + \mathrm{He}^4 + \mathrm{n}^1 \tag{2.101}$$

Neutrons come from the burning plasma as products of the deuterium-tritium fusion reaction, and are also generated in the liquid metal thanks to the moltiplication reaction with lead, Pb(n,2n).

The WCLL is a complex system, constitued by multiple regions of different materials. As a consequence, there are different processes that affect the behavior of tritium transport in the WCLL:

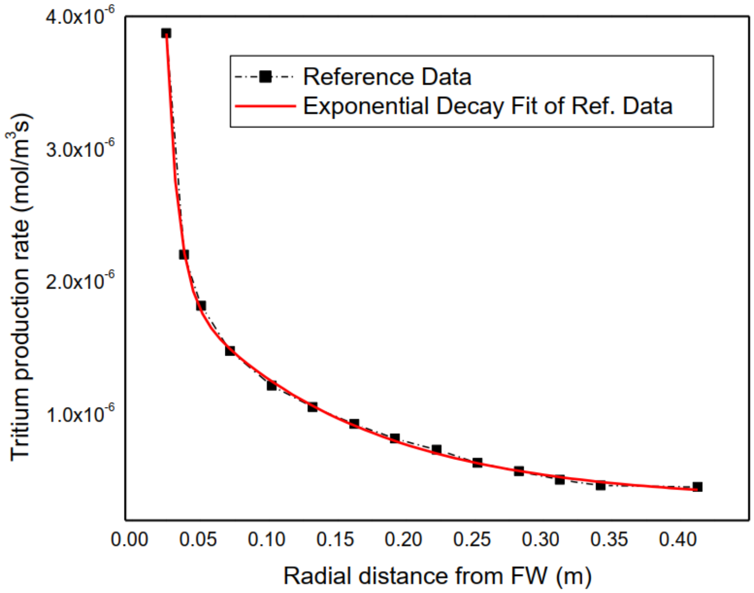

Figure 2.5: Radial profile of the tritium production in the PbLi for the HCLL [42].

1. Advection-diffusion of T into the lead-lithium eutectic alloy.
2. Adsorption/desorption of tritium at the LM/Eurofer interface.
3. Diffusion of tritium in the steel.
4. Recombination/dissociation of T at the structure/coolant interface.
5. Advection-diffusion of diatomic tritium in the coolant.

Considering advection and diffusion of tritium in the liquid metal, the assumption made is that tritium does not affect PbLi properties nor flow behavior, it is considerable as a passive scalar and magnetohydrodynamics is so independent from tritium transport [42]. The mass transport equation is:

$$\frac{\partial c_{T,LM}}{\partial t} + \overline{u_{LM}} \cdot \nabla c_{T,LM} = \nabla \cdot (D_{T,LM} \nabla c_{T,LM}) + \dot{S_{T,LM}} \tag{2.102}$$

where $c_{T,LM}$ is the tritium concentration in the liquid metal, $\overline{u_{LM}}$ is PbLi velocity, $D_{T,LM}$ is the tritium diffusivity in the liquid metal and $\dot{S_{T,LM}}$ is the molar tritium generation rate in the PbLi, that is space-dependent. The tritium generation rate is calculated from neutronics codes, and in absence of relations for the WCLL studied, in this work are used values obtained for the Helium Cooled Lead Lithium (HCLL) breeding blanket [41] [25].

At the LM/Eurofer interface Sievert's law (eqs. 2.103, 2.104) and continuity of partial pressures Eq. 2.105 are applied

$$c_{T,LM} = K_{S,LM} \sqrt{p_{T,LM}} \tag{2.103}$$

$$c_{T,Eu} = K_{S,Eu} \sqrt{p_{T,Eu}} \tag{2.104}$$

$$p_{T,LM} = p_{T,Eu} \tag{2.105}$$

from which the following relation can be obtained:

$$\frac{c_{T,LM}}{c_{T,Eu}} = \frac{K_{S,LM}}{K_{S,Eu}} \tag{2.106}$$

where $c_{T,Eu}$ is the tritium concentration in the Eurofer, $K_{S,LM}$ is the Sievert constant of tritium in the LM and $K_{S,Eu}$ is the Sievert constant of T in the structural Eurofer.

The adsorbed tritium diffuse through the solid structure. The diffusion equation can be written as:

$$\frac{\partial c_{T,Eu}}{\partial t} = \nabla \cdot (D_{T,Eu} \nabla c_{T,Eu}) \tag{2.107}$$

where $D_{T,Eu}$ is the tritium diffusivity in the Eurofer.

At the Eurofer/water interface flux continuity is applied, considering the dissociation and recombination phenomena:

$$(-D_{T_2,w} \nabla c_{T_2,w} + c_{T_2,w} \cdot \overline{u_w}) \cdot \widehat{n}|_{w/Eu} = -k_d p_{T_2,w} + k_r c_{T,Eu}^2 \tag{2.108}$$

$$(-D_{T,Eu} \nabla c_{T,Eu}) \cdot \widehat{n}|_{Eu/w} = 2(k_d p_{T_2,w} - k_r c_{T,Eu}^2) \tag{2.109}$$

$c_{T_2,w}$ is the diatomic tritium concentration in the water, $D_{T_2,w}$ and $D_{T,Eu}$ are, respectively, the diffusion coefficients of tritium in water and Eurofer, $p_{T_2,w}$ is the tritium partial pressure in the water, k_d is the dissociation coefficient and k_r is the recombination coefficient.

Advection and diffusion of tritium in the coolant water is described by the mass transport equation:

$$\frac{\partial c_{T_2,w}}{\partial t} + \overline{u_w} \cdot \nabla c_{T_2,w} = \nabla \cdot (D_{T_2,w} \nabla c_{T_2,w}) \tag{2.110}$$

The inlet boundary conditions in all the i domains are set to zero

$$c_i = 0 \tag{2.111}$$

while at the outlet it is assumed that the diffusion contribution is much smaller than the convective contribution (perfect extraction from the blanket):

$$\widehat{n} \cdot D_i \nabla c_i = 0 \tag{2.112}$$

The initial condition have been set to zero.

This model gives as output the concentration of tritium. It is also interesting to express tritium losses, that are defined as the ratio between the tritium permeated through the Eurofer structures (pipes, baffle) to the total tritium generated in the PbLi [43]:

$$\Phi_{WCLL} = 100 \frac{\iint J_{perm} dA_i}{\iiint \dot{S}_{T,LM} dV_{LM}} \tag{2.113}$$

where Φ_{WCLL} are the tritium losses in the WCLL, J_{perm} is the total flux that permeates from the PbLi domain to the Eurofer domain through the A_i surfaces. Another quantity investigated is the tritium inventory $I_{WCLL,i}$ for the WCLL in the i-th domain:

$$I_{WCLL,i} = M_T \iiint c_i dV_i \tag{2.114}$$

where M_T is the tritium atomic weigth, V_i is the volume of the i-th domain.

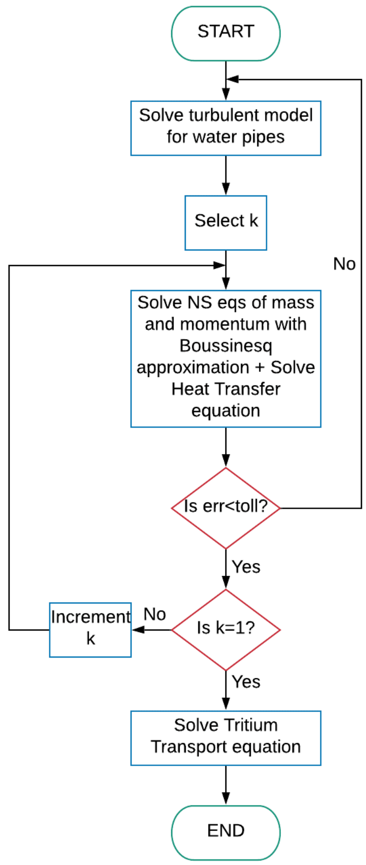

Figure 2.6: Flow chart of the solution strategy for new WCLL geometry.

2.3 Solving magnetohydrodynamics and tritium transport

The solution for magnetohydrodynamics and tritium transport is obtained using COMSOL multiphysics. As already said, thanks to the fact that tritium does not affect the flow, transport can be decoupled from the other physics.

As expressed in Fig. 2.6, in a first step the turbulent model is solved for the water pipes. Then fluid dynamics, electromagnetism and heat transfer are solved together iteratively, exploiting the gravity ramping technique (described in Section 4.1.2). The temperature and velocity profiles obtined are used as input for the tritium transport model, that is then solved.

Chapter 3

Benchmark of the code

Smolentsev *et al.* [34] proposed a method for verification and validation[1] (V&V) of MHD codes, consisting of a series of benchmark problems whose results are known from experimental data or trusted analytical and numerical solutions. In particular, the five problems cover a wide range of magnetohydrodynamic flows which are of interest for fusion applications: a) 2D fully developed laminar steady MHD flow, b) 3D laminar, steady developing MHD flow in a non-uniform magnetic field, c) MHD flow with heat transfer (magnetoconvection), d) quasi-two-dimensional MHD turbulent flow and e) 3D turbulent MHD flow.

In this work Smolentsev procedure is taken as reference, and the first three cases, involving laminar flows, are solved. For the first two benchmarks, the problems selected by Smolentsev are considered, while for case c) (magnetoconvection), the problems selected are the one proposed by Di Piazza and Buhler [26], that are particularly interesting for the WCLL analysis.

3.1 2D fully developed MHD flow

An electrically conducting fluid flows in a rectangular duct and it is subject to a uniform transverse magnetic field. The problem is illustrated in Section 2.1.1, and was analytically solved by Shercliff [33] for a non-conducting duct and by Hunt [16] for a duct with electrically conducting walls. In both cases the flow forms two Harmann layers at the walls perpendicular to the magnetic field and two side layers parallel to the magnetic field, with thickness scaling as $1/Ha$ and $1/Ha^{1/2}$, respectively. In Figure **??**, the dimensionless velocity profile for the case Ha = 500 is reported as example for both Schercliff and Hunt cases. In the case of electrically conducting walls, high-velocity jets near the side walls are produced, with width that also scales with $1/Ha^{1/2}$, forming a “M-shaped” velocity profile, shown in Figure 3.1b. The nature of this characteristic velocity profile will be explained in the subsection 3.1.2.

The problem, for both cases, is solved in three different ways. Analytically, solving the equations obtained in Section 2.1.1 (eqs. 2.53, 2.56, 2.62, 2.63 and 2.68). Numerically, using a MATLAB® code that solves the system of ordinary differential equations 2.51 and 2.52 with their respective boundary conditions. Lastly, the problem is solved using the software COMSOL Multiphysics®. To minimize the computational cost, considering that the solution is symmetric in both x and y axis, just a quarter of domain is considered, applying proper boundary conditions. In particular, for fluid dynamics:

$$\overline{u} \cdot \widehat{n} = 0 \tag{3.1}$$

where $\widehat{n}$ is the unit vector perpendicular to the boundary and directed outward. For electromagnetism symmetry boundary conditions are electrical insulation

$$\overline{J} \cdot \widehat{n} = 0 \tag{3.2}$$

[1]Briefly, verification is the process of determining if the code is “solving the equations right”, validation is the process of determining if the code is “solving the right equations”.

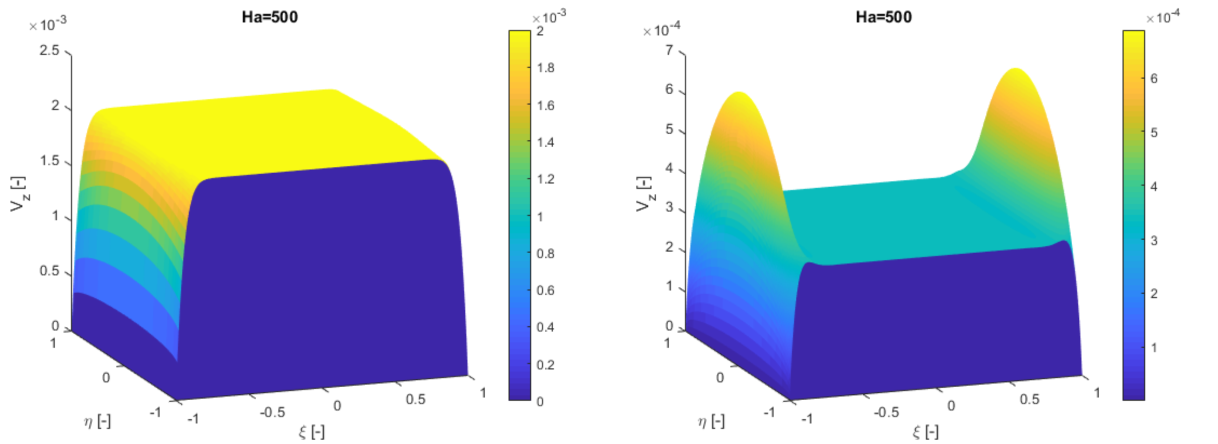

(a) Shercliff's case.

(b) Hunt's case.

Figure 3.1: Dimensionless velocity profile for $Ha = 500$. The magnetic field is directed along η.

in the side perpendicular to the magnetic field, and $\phi = 0$ in the side parallel to $\overline{B}$.

An example of mesh used is shown in Figure 3.2, similar to the one proposed by Sahu *et al.* [32]. Elements are generated in x and y direction with a geometric distribution, maximizing the number of cells in the side and Harmann layers. The problem is invariant in z, so only one element is used in the direction of the flow.

Analytical, numerical with Matlab and COMSOL solutions are compared to those reported by Smolentsev. The chosen parameter of comparison is the dimensionless flow rate $\widetilde{Q}$, obtained integrating the dimensionless velocity over the channel's cross section. This, being an integral parameter, is better suited as a comparison value than the local velocities. The described cases have been developed for different Ha number: 500, 5000, 10000 and 15000.

3.1.1 Shercliff's case

Shercliff's case is now considered. In Fig. 3.3 is presented the dimensionless velocity profile for $Ha = 500$ and $Ha = 15000$. It is evident the reduction of the velocity and the side layer width with the increase of Ha.

In Table 3.1 is shown the comparison of the dimensionless volumetric flow rate $\widetilde{Q}$ between the benchmark value and our results. The relative error, defined in percentage as

$$\epsilon = \left| \frac{\widetilde{Q_S} - \widetilde{Q}}{\widetilde{Q_S}} \right| \times 100 \tag{3.3}$$

where $\widetilde{Q_S}$ is Smolentsev's value and $\widetilde{Q}$ is the volumetric flow rate obtained by our calculations, is small ($<<$ 1%) for the analytical and numerical solutions. For $Ha = 500$ and $Ha = 5000$, solved with COMSOL®, the error is still small (0.014% and 0.05% respectively), but it increases for the other two cases, and it is maximum for $Ha = 15000$, with a value of 4.07%. For the present work results with an error $< 10\%$ are considered reasonable, so this is more than acceptable. The main reasons why lower errors were difficult to obtain and why they get bigger with Ha is that convergence is slower as Ha is increased and c_w is reduced [37], and for Shercliff's case c_w is zero for all the four walls.

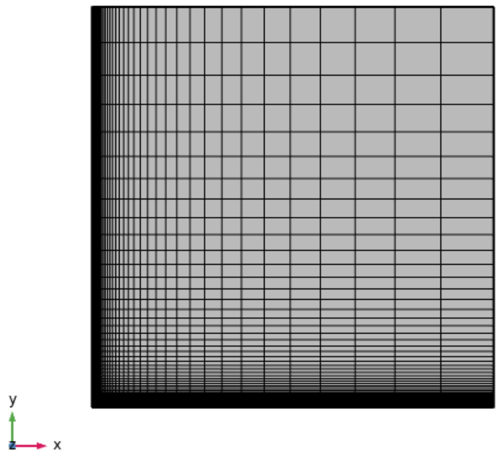

Figure 3.2: Typical mesh used in COMSOL multiphysics® solution.

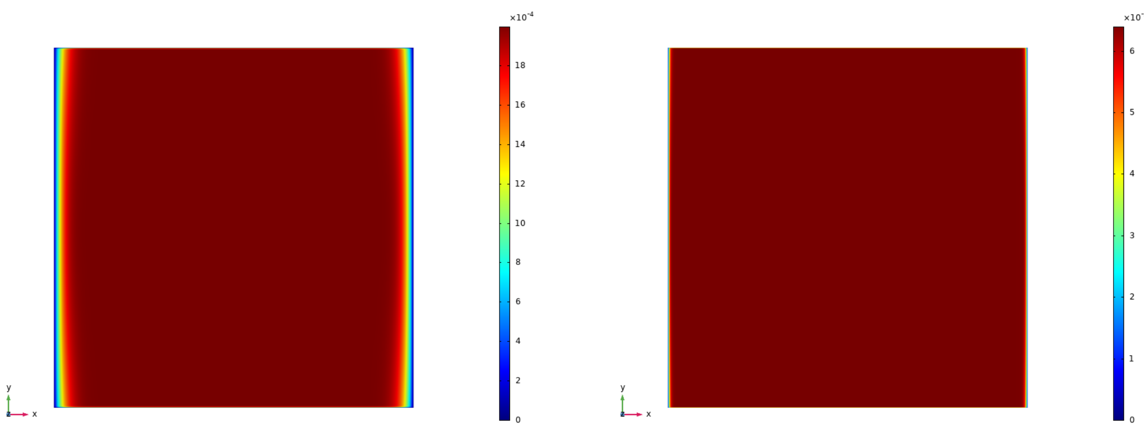

(a) $Ha = 500$.

(b) $Ha = 15000$.

Figure 3.3: Dimensionless velocity profile for Shercliff's case and Harmann numbers 500 and 15000.

Ha	Analytical	Error [%]	Numerical	Error [%]	COMSOL®	Error [%]
500	7.6799×10^{-3}	0.0015%	7.6565×10^{-3}	0.3062%	7.6691×10^{-3}	0.1419%
5000	7.9020×10^{-4}	0.0006%	7.8642×10^{-4}	0.4787%	7.9062×10^{-4}	0.0532%
10000	3.9655×10^{-4}	0.0121%	3.9461×10^{-4}	0.4777%	3.9119×10^{-4}	1.3392%
15000	2.6479×10^{-4}	0.0045%	2.6348×10^{-4}	0.4979%	2.5401×10^{-4}	4.0748%

Table 3.1: Obtained values of dimensionless volumetric flow rate $\widetilde{Q}$ for Shercliff's case.

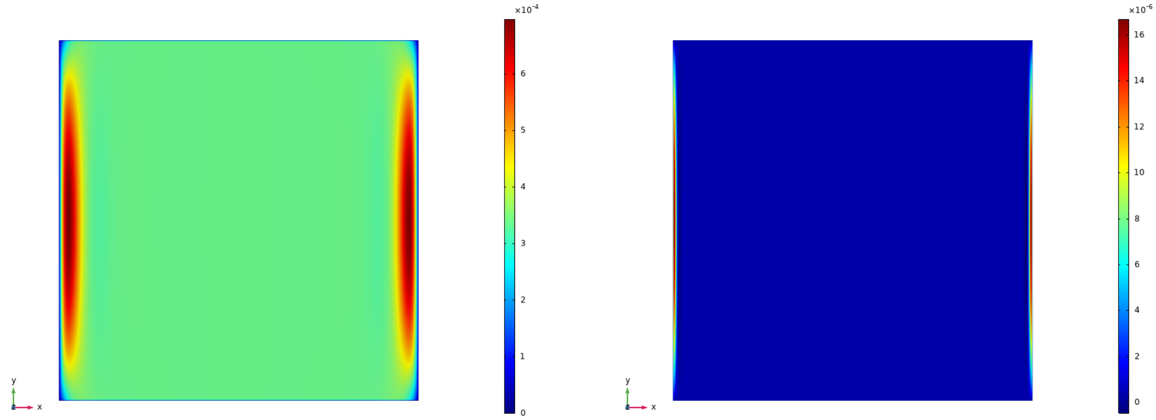

(a) $Ha = 500$. (b) $Ha = 15000$.

Figure 3.4: Dimensionless velocity profile for Hunt's case and Harmann numbers 500 and 15000.

Ha	Analytical	Error [%]	Numerical	Error [%]	COMSOL®	Error [%]
500	1.4053×10^{-3}	0.0244%	1.4013×10^{-3}	0.2631%	1.4082×10^{-3}	0.2278%
5000	1.9066×10^{-5}	0.0222%	1.8987×10^{-5}	0.4328%	1.9035×10^{-5}	0.1835%
10000	5.1616×10^{-6}	0.1440%	5.1407×10^{-6}	0.5482%	5.1349×10^{-6}	0.6597%
150000	2.4174×10^{-6}	0.3129%	2.4076×10^{-6}	0.7177%	2.4096×10^{-6}	0.6351%

Table 3.2: Obtained values of dimensionless volumetric flow rate $\widetilde{Q}$ for Hunt's case.

3.1.2 Hunt's case

For the Hunt's case the Harmann walls have a conductivity ratio $c_w = 0.01$. The value has been selected following Smolentsev's procedure. In Fig. 3.4 is shown the dimensionless velocity profile. The "M-shaped" profile is evident, and it is explained by the fact, as noticeable from Figure 3.5, that in the side layers the y component of the current density is dominant, and being parallel to the magnetic field, it does not contribute to the Lorentz force $\overline{J} \times \overline{B}$ that acts against the flow. In the core region J_y vanishes, while J_x is big, leading to a greater force.

From figure 3.4 it is also evident that the width of the spikes near the side walls reduces for increasing Ha numbers.

Table 3.2 is shows the comparison of the dimensionless volumetric flow rate $\widetilde{Q}$ between the benchmark value and our results. For Hunt's case it was easier to obtain smaller errors and ϵ is less than 1% in every computation. Particularly, it is in the order of 0.1% for Hartmann 500 and 5000, and reaches the maximum value of 0.635% for $Ha = 15000$.

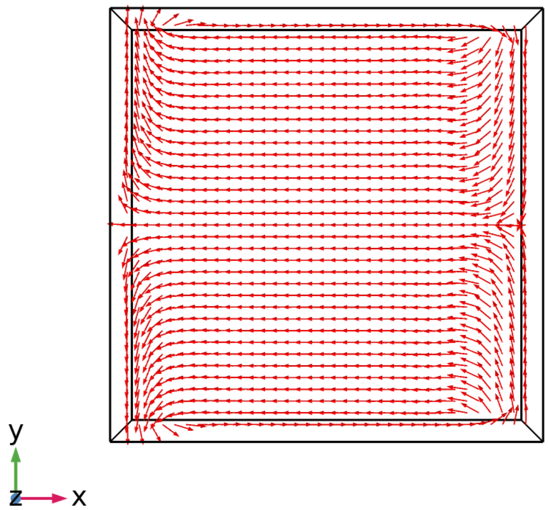

Figure 3.5: Current density profile for Hunt's case at $Ha = 500$. $\overline{B}$ is directed in the y direction. It is evident that the leading component of $\overline{J}$ in the core is perpendicular to the magnetic field, while in the side layers J_x is small.

3.2 3D developing MHD flow in a non-uniform magnetic field

In the second benchmark case a conducting fluid flows in a square duct in the presence of a non-uniform magnetic field at the exit from a magnet. This case was investigated experimentally at the Argonne National Laboratory with ALEX (Argonne's Liquid Metal Experiment) facility [27] [29] [28]. The system employed euthetic NaK as working fluid in a room temperature closed loop. Maximum Hartmann numbers attainable were up to 6.6×10^3 with interaction parameters in the range of $10^3 - 10^5$, values interesting for the development of liquid metal breeding blankets.

The solution for this problem is obtained with COMSOL multiphysics. Equations are those solved for the 2D fully developed MHD flow case, explained previously in Section 3.1. The only difference is that now the magnetic field changes in the direction of the flow x. This requires the additional discretization of the domain in the x direction, and a typical mesh used in shown in 3.6. The symmetry of the problem is exploited, and, again, only a quarter of duct's cross section is considered. The mesh is similar to the previous cases in directions y and z, and a symmetric distribution of elements is adopted in the direction of the flow, maximizing the number of cells in the central region, where the B field is changing the most.

The parameters adopted for the study are $Ha = 2900$, $N = 540$ and $c_w = 0.07$, as proposed by Smolentsev [34]. The quantity selected for the comparison with the experimental results is the dimensionless transverse pressure difference, that is the pressure difference developed between the centerline of the duct and the wall in the direction perpendicular to both the magnetic field and the flow, scaled by σLUB_0^2 and it is a function of x.

Results are presented in Figure 3.7. In 3.7a is shown the magnetic field profile scaled by B_0 and the transverse pressure difference obtained by Picologlou *et al.* [27] experimentally and numerically, both expressed as a function of the dimensionless coordinate x/L. In 3.7b is shown the solution obtained with the COMSOL tool. It can be seen that the behavior is the same, but there is a slight difference in the numerical value of the Δp. In the experimental case it has a maximum value of ~ 0.05, while in COMSOL solution it has a maximum value of 0.04. This discrepancy depends on different factors. Firstly, it was not possible to have the exact profile of the magnetic field, that was exported manually from Fig. 3.7a.

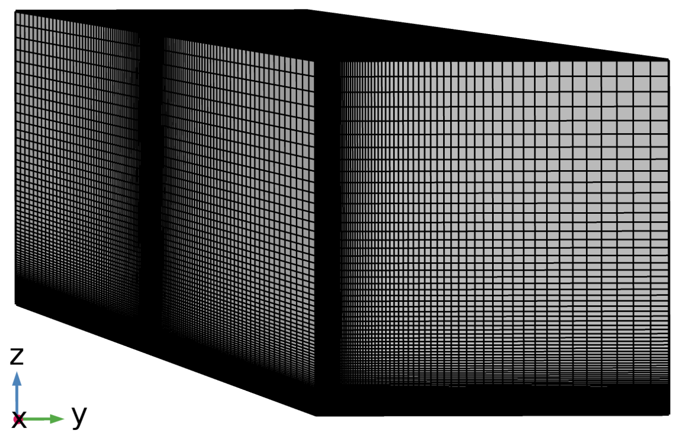

Figure 3.6: Typical mesh used in COMSOL multiphysics® solution.

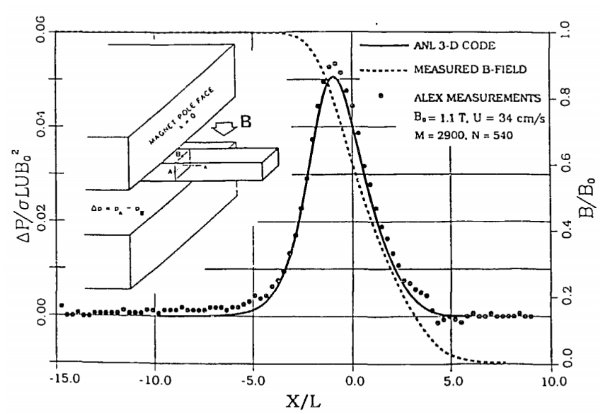

(a) ALEX experiment measurements and numerical solution [27].

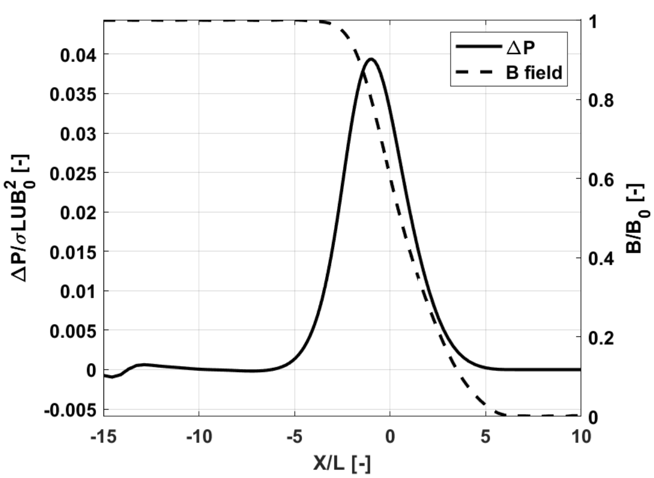

(b) COMSOL solution.

Figure 3.7: Magnetic field and transverse pressure difference profile as a function of x/L. M indicates the Hartmann number, while N is the interaction parameter.

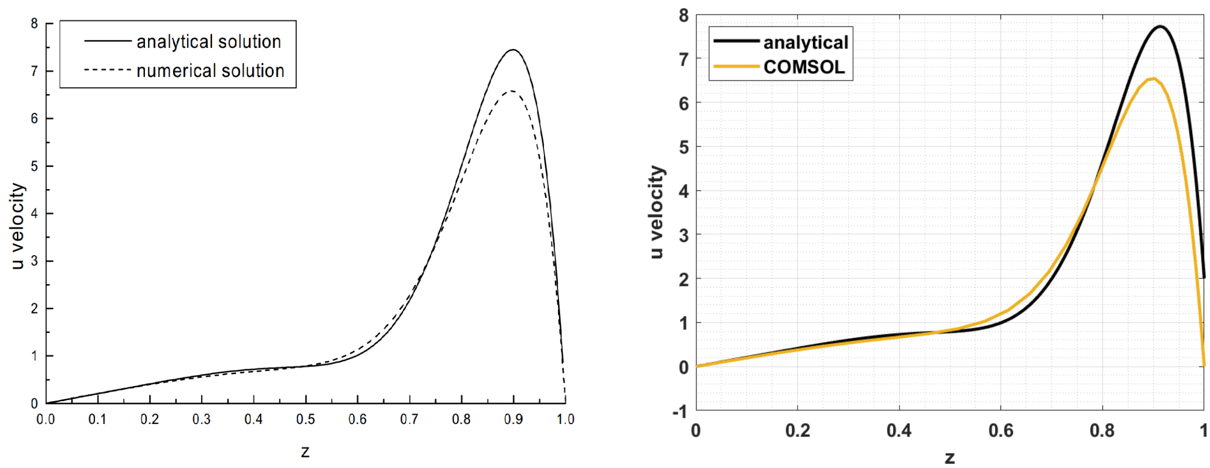

(a) Di Piazza and Buhler solutions [26].

(b) Analytical and COMSOL solutions obtained in the present work.

Figure 3.8: Comparison between analytical and numerical solutions of velocity profile for a differentially heated duct in the $y = 0$ plane, with $T = z$, $Ha = 100$ and $c_w = 1$. Only half duct is considered.

Another source of error derives from the fact that it was not possibile to increase too much the number of elements due to limitations in computational resources.

3.3 Magnetoconvection

The third case proposed by Smolentsev is now introduced with reference to the work proposed by Di Piazza and Buhler. The managetoconvection problem is mathematically described in Section 2.1.2. In particular, the two cases introduced in Section 2.1.2, differentially and uniformely heated duct, are solved analytically and numerically employing a COMSOL multiphysics code.

3.3.1 Differentially heated duct

The two boundaries at $z = -1$ and $z = 1$ are kept at different temperatures and there is not internal heat generation, so the temperature profile becomes linear.

The analytical solution is obtained solving equations from 2.87 to 2.92. The problem is 2D, and COMSOL solution is found using a mesh similar to Fig. 3.2.

In Fig. 3.8 it can be seen the comparison of the velocity profile for Di Piazza and Buhler (Figure 3.8a) and the analytical and COMSOL (Figure 3.8b) solutions. Only half the duct in the plane $y = 0$ is presented for $Ha = 100$ and $c_w = 1$. Velocity exhibits a linear profile in the core, where viscous effects are negligible and buoyancy is balanced by Lorentz forces. The side layer is governed by viscous effects and by the current pattern, and high velocity jets are produced.

A qualitative evaluation has been carried out. The agreement between DP&B solution and the one presented in this work is quite good, while for both graphs the analytical and numerical solutions do not perfectly match in the side layers. This is due the fact that the asymptotic approach, followed to obtain the analytical solution, does not apply exactly because relevant currents flow parallel to the wall within the side layer [26].

In Fig. 3.9 the potential profile is presented, and the gradient in the side layer sustain the velocity peak.

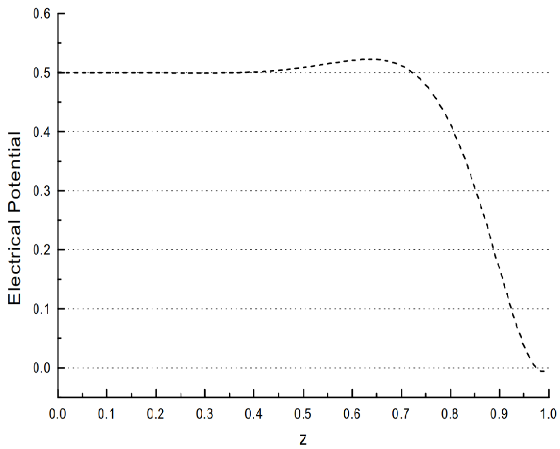

(a) Di Piazza and Buhler solution [26].

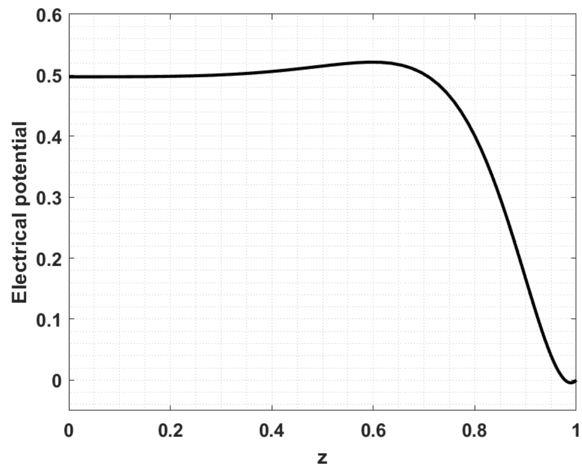

(b) COMSOL solution.

Figure 3.9: Potential profile for a differentially heated duct in the plane $y = 0$, with $T = z$, $Ha = 100$ and perfectly conducting walls.

A sensitivity analysis, changing the wall conductance ratio, is shown in Fig. 3.10, for $Ha = 100$. It is interesting to notice that for the lower values of c_w the damping effect of magnetohydrodinamics is less evident, while in the core region the solution is still dominated by Lorentz forces and exhibits a linear behavior, with a slope of $\sim Ha$ for the perfectly insulating walls case [6]. In the lower conductivity cases, jets are not present. This is due the fact that for low values of c_w the side layer becomes better conducting than the side walls and high current jets are now present in the layers, parallel to the side walls. They are also parallel to $\overline{B}$, so they do not interact with the magnetic field, therefore the electric magnetic forces in the side layers become negligible and the dominant effect is due to viscous dissipation.

Again a good agreement between DB&B solution and the one obtained for this work is noticeable, proving the accuracy of the codes developed.

3.3.2 Uniformly heated duct

For the uniformly heated duct, internal heat generation is present and the boundary at $z = -1$ and $z = 1$ are kept at an equal temperature, so the temperature profile established is parabolic. In a pure fluid dynamic case with buoyancies the flow goes up in the centre of the duct and down close to the walls kept at the constant temperature, considering the other walls adiabatic. In the MHD case, for high wall conductivity ratios, the additional forces damp the velocity profile in the core region, as can be seen in Figure 3.11 for $Ha = 100$, and velocity jets are present in the side layers. For small values of c_w, jets are no more present, like in the case of differentially heated duct, and the solution at the side layers is dominated by viscous effects.

A similar sensitivity analysis is shown in Fig. 3.12, for $Ha = 1000$. It is evident that for higher Hartmann numbers the thickness of jets decreases, scaling with $\sim Ha^{-1/2}$ [26].

Figure 3.13 shows the normal wall current, the interval $1 < \zeta_{wall} < 3$ is referred to the Hartmann walls, while the others to the side walls. The selected value of Ha is 1000 and $\overline{J} \cdot \widehat{n}$ for different values of c_w is displayed. It can be seen that is small in the side walls for small wall conductance ratio. Like in the differentially heated duct case, the side layers become better conducting than the side walls and high currents flow in the layers parallel to the walls and to the magnetic field, giving little contribution to Lorentz forces.

All the displayed figures show that results obtained with the COMSOL multiphysics tool are in good agreement with the solutions of Di Piazza and Buhler, emphasizing the reliability of the code developed.

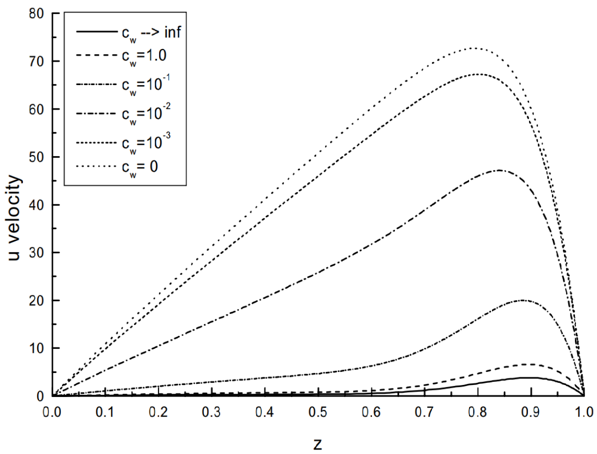

(a) Di Piazza and Buhler solutions [26].

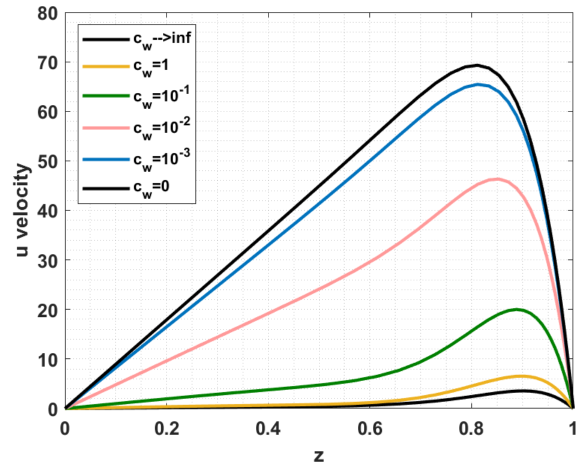

(b) COMSOL solution.

Figure 3.10: Velocity profiles for half duct in the plane $y = 0$ for a differentially heated duct with $T = z$, $Ha = 100$ and for different values of the wall conductivity.

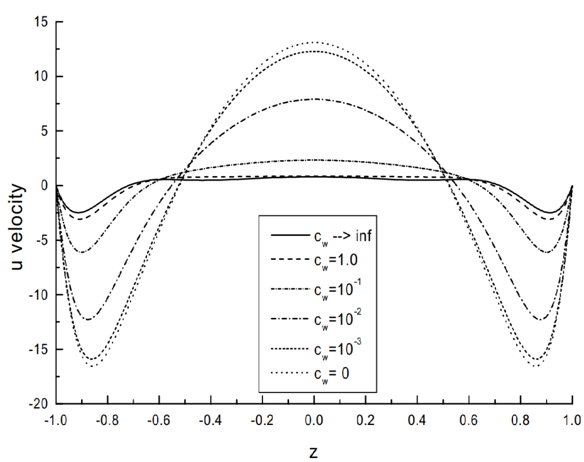

(a) Di Piazza and Buhler solutions [26].

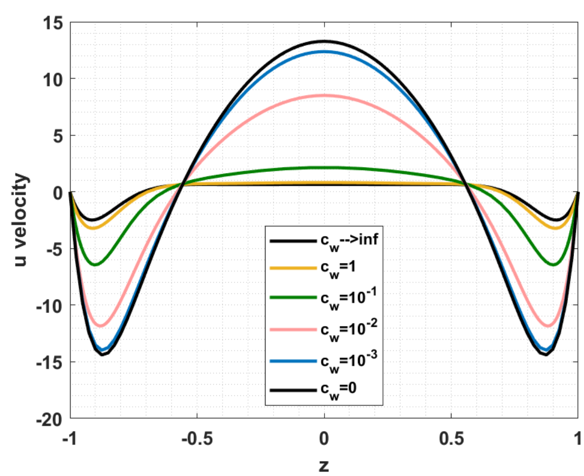

(b) COMSOL solution.

Figure 3.11: Velocity profiles in the plane $y = 0$ for a uniformly heated duct with $Q = 1$, $Ha = 100$ and for different values of the wall conductivity.

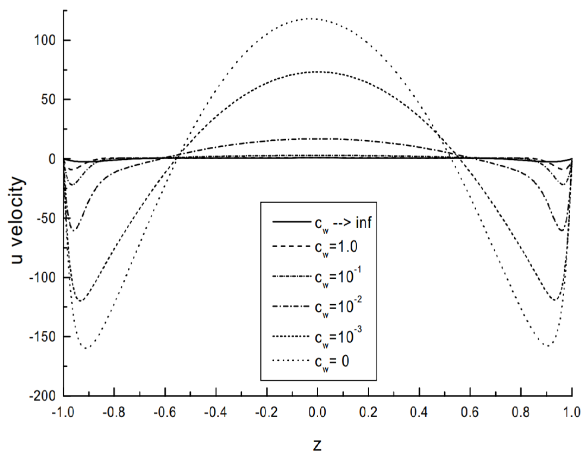

(a) Di Piazza and Buhler solutions [26].

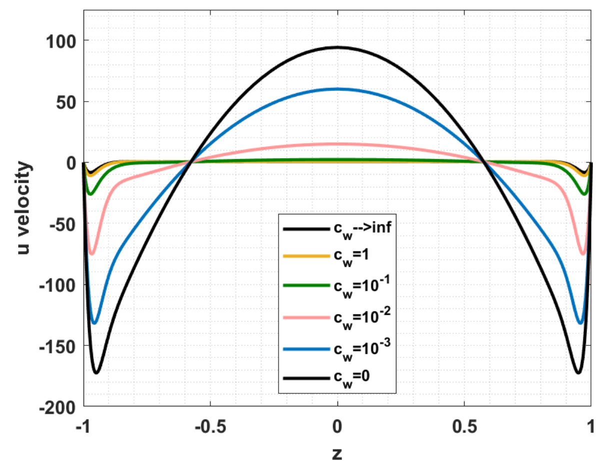

(b) COMSOL solution.

Figure 3.12: Velocity profiles in the plane $y = 0$ for a uniformly heated duct with $Q = 1$, $Ha = 1000$ and for different values of the wall conductivity.

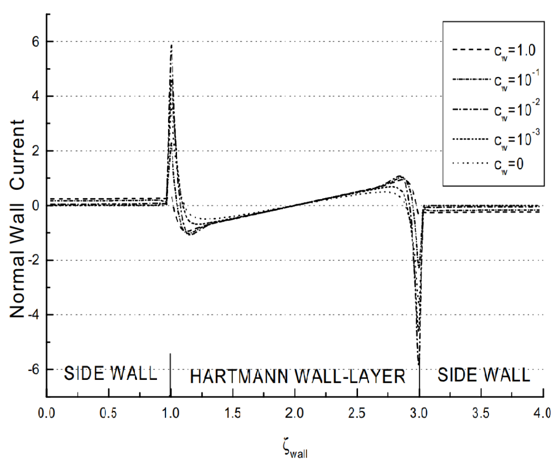

(a) Di Piazza and Buhler solutions [26].

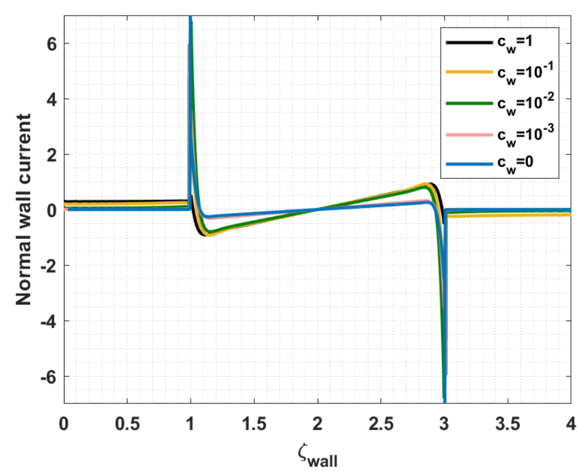

(b) COMSOL solution.

Figure 3.13: Currents normal to the walls in an internally heated duct with $Q = 1$, $Ha = 1000$ and different values of c_w.

Chapter 4

Results

The analysis of the WCLL model is now shown. Due to the complexity of the geometry, the minimum considerable domain is half the module. The CFD model is solved for this domain, considering buoyancy contribution. The magnetohydrodynamic effect and tritium transport are only included in three simplified models of the WCLL. In particular, a straight, rectangular duct with zero, one and two coolant tubes is analyzed. Both the pure MHD and the magnetoconvection case are solved.

4.1 CFD analysis

4.1.1 Grid convergence study and mesh selection

To ensure a minimum discretization error due to insufficient spatial resolution, a grid convergence study is performed, using the grid convergence index (GCI) method, as suggested by the ERCOFTAC Best Practice Guidelines [10] [12] [30]. Three different grids are selected and are indicated as M1, M2 and M3, where M1 is the most fine and M3 the coarser. They should have geometrically similar cells with a grid refinement factor:

$$r = \frac{h_{coarse}}{h_{fine}} \tag{4.1}$$

bigger than 1.3, where h_{coarse} and h_{fine} are the rapresentative cell size of the coarser and finer meshes, respectively. h is defined as:

$$h = \left(\frac{1}{N} \sum_{i=1}^{N} \Delta V_i \right)^{1/3} \tag{4.2}$$

where N is the number of elements and ΔV_i is the volume of the i-th cell. The grid refinement must be done systematically, with a structured refinement even if the grid is unstructured. In the present work, the meshes developed are hybrid, consisting in both structured and unstructured meshes. In the refinement process, homogeneous refinements for the cells are obtained using the built-in function of COMSOL multiphysics, as shown in Fig. 4.1. The CFD model is solved using these meshes.

Twenty variables, local and global, are selected to carry out the GCI calculations, presented in Table 4.1. The inlet and outlet locations of PbLi exit are identified by a matrix notation, where the rows indicate the entrance/exit whereas the columns identify the position moving in toroidal direction. The results of the method are shown in Fig. 4.2.

Low values of GCI indicate the grid independency, and for this work a GCI smaller than 10% is acceptable. Considering the results and the computational time needed to perform the calculations, the mesh M2 is chosen as reference mesh, and is presented next (Fig. 4.3, 4.4 and 4.5).

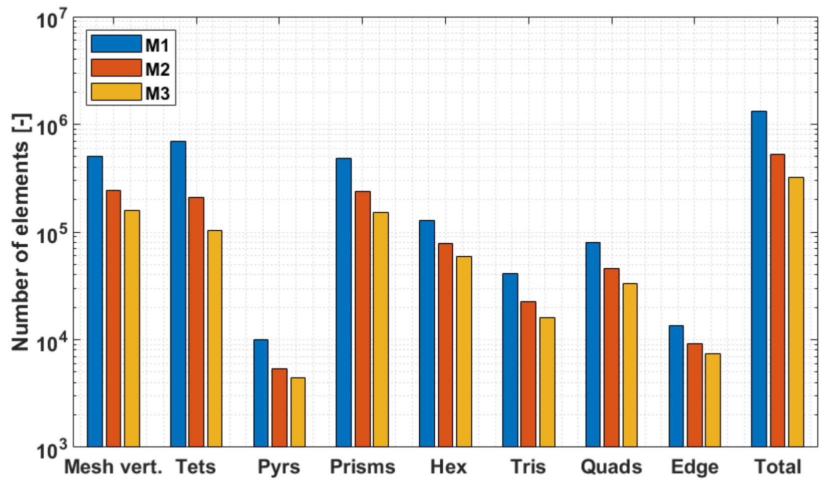

Figure 4.1: Mesh elements trend for M1, M2 and M3. From left to right: mesh vertices, tetrahedral elements, pyramids elements, prisms elements, hexaedra elements, triangles, quads, edge elements and total number of elements.

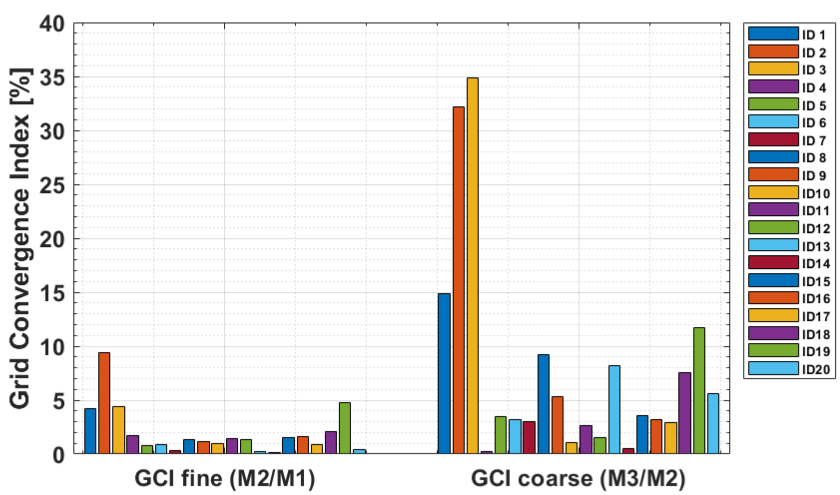

Figure 4.2: Grid convergence index for the three different meshes.

ID	Description	Local	Global
1	Velocity on the middle of PbLi exit surface [1, 1]	X	
2	Velocity on the middle of PbLi exit surface [1, 2]	X	
3	Velocity on the middle of PbLi exit surface [1, 3]	X	
4	Temperature on the middle of PbLi exit surface [1, 1]	X	
5	Temperature on the middle of PbLi exit surface [1, 2]	X	
6	Temperature on the middle of PbLi exit surface [1, 3]	X	
7	Average velocity on PbLi exit surface [1, 1]		X
8	Average velocity on PbLi exit surface [1, 2]		X
9	Average velocity on PbLi exit surface [1, 3]		X
10	Average temperature on PbLi exit surface [1, 1]		X
11	Average temperature on PbLi exit surface [1, 2]		X
12	Average temperature on PbLi exit surface [1, 3]		X
13	Average velocity on PbLi domain		X
14	Average velocity on water domain		X
15	Average temperature on PbLi domain		X
16	Average temperature on water domain		X
17	Average temperature on Eurofer domain		X
18	Max temperature on PbLi domain		X
19	Max temperature on water domain		X
20	Max temperature on Eurofer domain		X

Table 4.1: Variables selected for the GCI method.

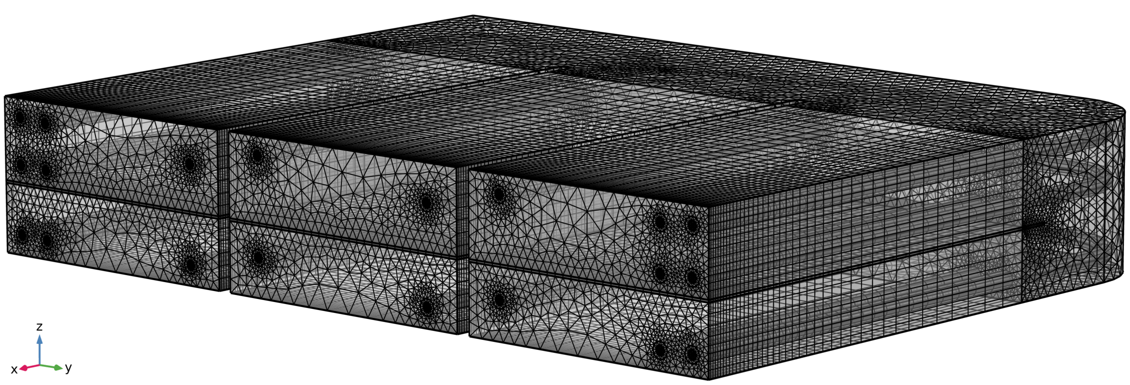

Figure 4.3: Mesh of the full domain.

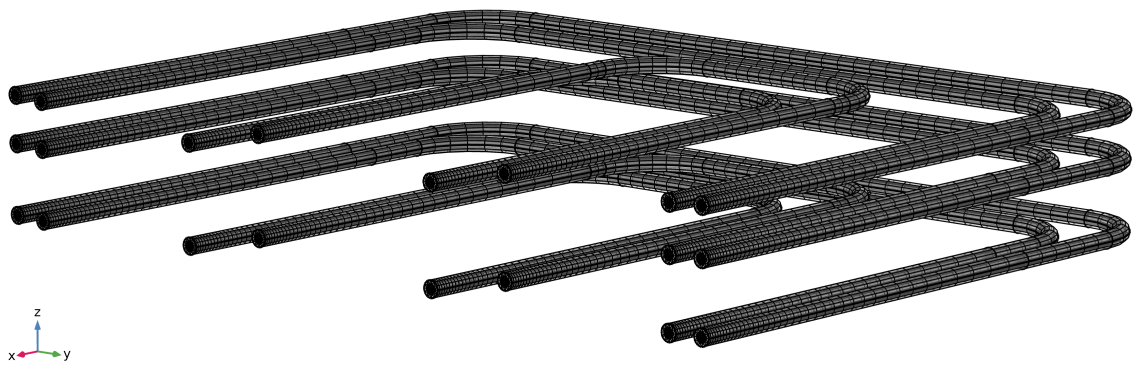

Figure 4.4: Mesh of the tubes domain.

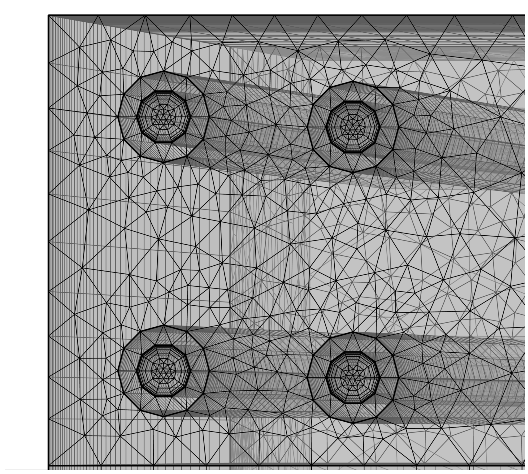

Figure 4.5: Particular of the mesh of the water pipes.

4.1.2 CFD results

With reference to the Figure 4.3, the PbLi enters in the three rectangular duct on the bottom of the module and exits from the three on the top. The boundary conditions are imposed average velocity in the inlet and null pressure in the outlet. Water enters in the eight tubes on the left, removes the heat from the blanket and exits from the eigth tubes on the right. BCs are equivalent to the one for the PbLi. The other conditions are no slip in all the other boundaries. Fluid dynamics is solved using the $k-\omega$ turbulence model in both PbLi and water domains.

Heat transfer is solved considering adiabatic conditions in all the external surface excluded the boundaries facing the first wall, on which a heat flux is imposed, that is a conservative assumption. The volumetric heat generation in the PbLi, water and Eurofer is included, produced by the incoming particles and function of the radial coordinate.

Two cases are considered, one without buoyancies and one considering buoyancies under the Boussinesq hypothesis, for which density variations affects only the gravity term in Navier-Stokes equations. In the buoyancy case, in order to deal with the high non-linearity of the system of partial differential equations, the gravity term was included using the gravity ramping technique. The equations are solved iteratively increasing step-by-step a coefficient k, multiplied to the gravity term, from 0 (no buoyancy case) to 1 (buoyancy case). The momentum equation becomes

$$\rho_0 \left(\overline{u} \cdot \nabla\right) \overline{u} = -\nabla p + \mu \nabla^2 \overline{u} + k \left(\rho_0 + \Delta\rho\right) \overline{g} \tag{4.3}$$

where ρ_0 is the reference density. This procedure is shown in Fig. 2.6 of Section 2.3.

Considering the no buoyancy case, in Fig. 4.6 the PbLi velocity field in the radial-poloidal plane placed in the half of the module is presented. The arrows indicate the stream direction, and are proportional to the velocity. In 4.7 the temperature field is shown. The peak temperature is placed near the first wall, where the heat flux is incoming and the volumetric heat generation rate is maximum.

Now the buoyancy case results are shown. In Fig. 4.8 the velocity profile is presented. As can be seen, there is a spot of high velocity near the exit and there is an incoming flow from the outlet. This backflow phenomenon may be due to the low velocity of the PbLi circulating in the blanket and to the dominant effect that buoyancy has on the flow behavior, that can be seen comparing Figures 4.6 and 4.8. It may be also due to the boundary conditions adopted, and further investigations are needed. In Figure 4.9 the temperature field is shown. The peak temperature is extremely smaller than in the no buoyancy case.

Comparing the two cases investigated, it is evident that buoyancy plays a major role, smoothing the temperature field, and cannot be neglected.

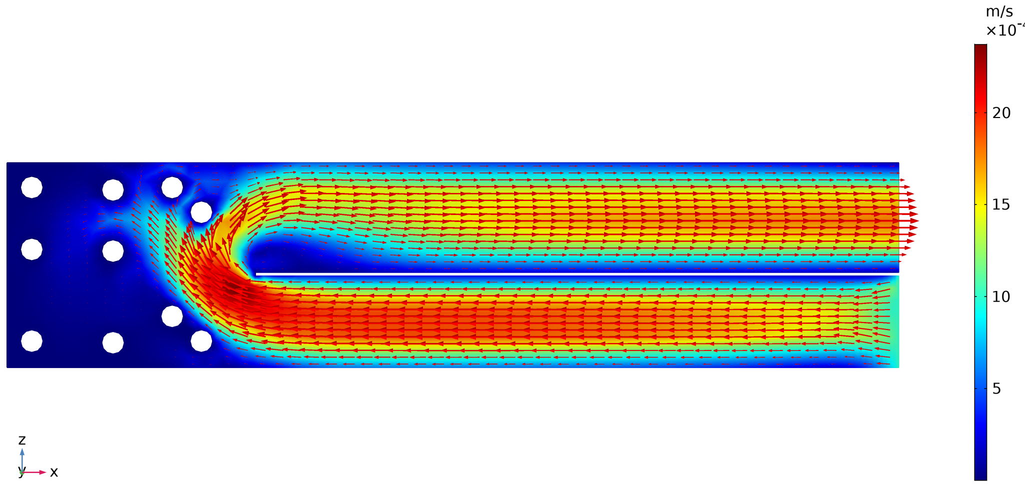

Figure 4.6: Velocity profile for the case without buoyancy.

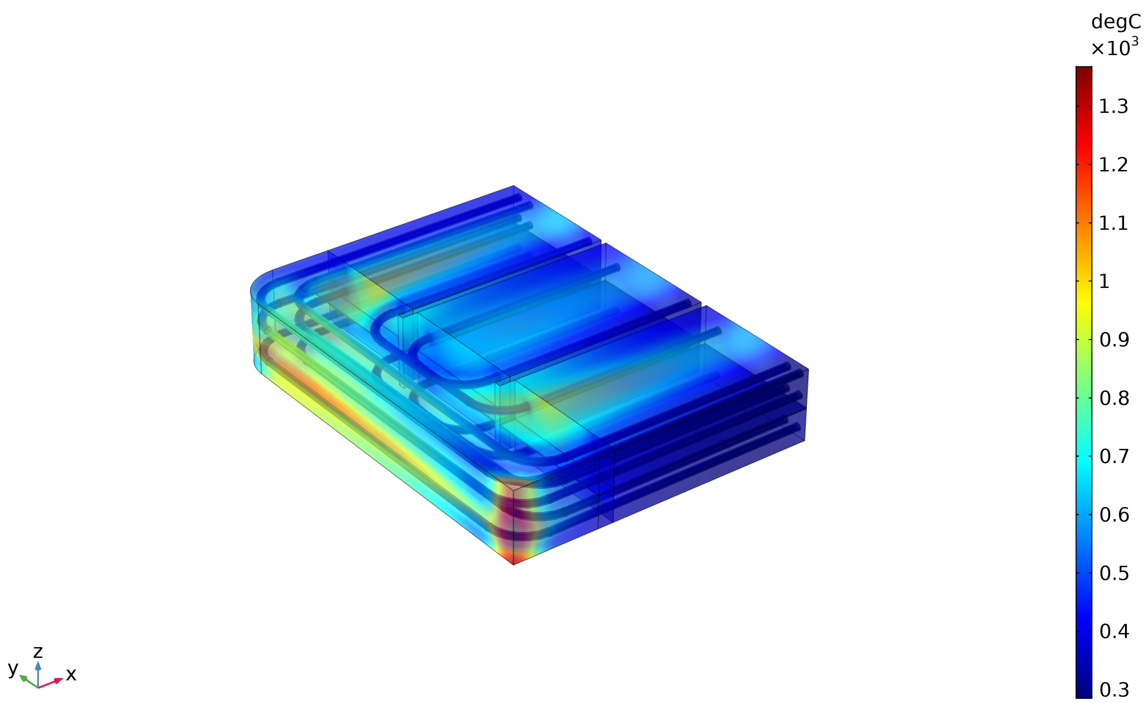

Figure 4.7: Temperature profile for the case without buoyancy.

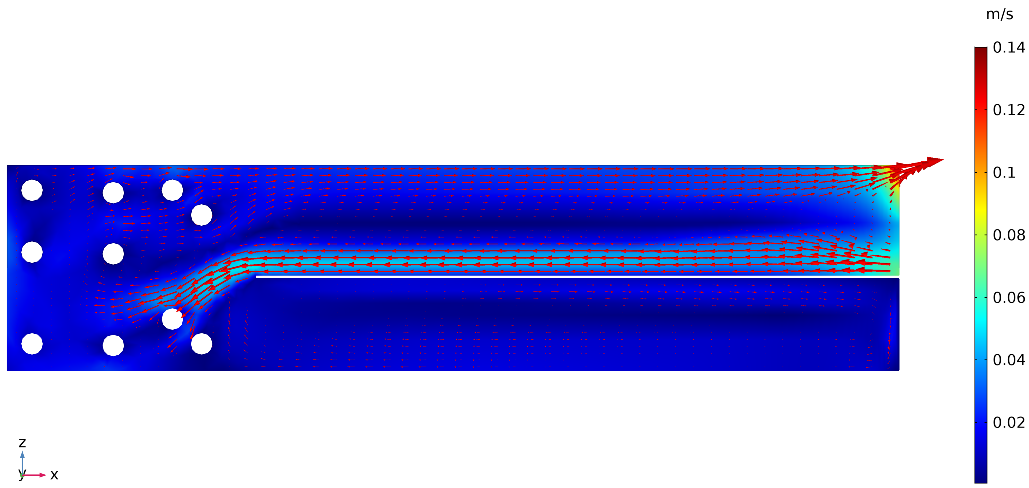

Figure 4.8: Velocity profile for the buoyancy case.

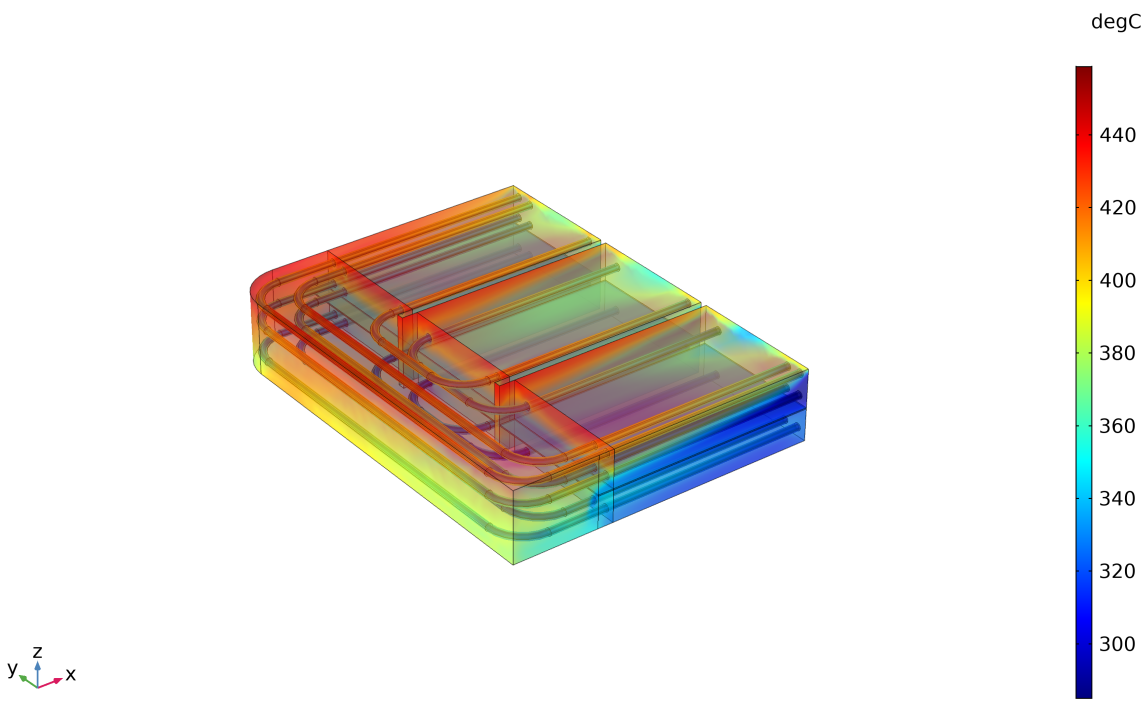

Figure 4.9: Temperature profile for the buoyancy case.

4.2 MHD and tritium transport analysis

The introduction of additional physics to the already complex CFD model requires a massive computational cost. To solve MHD and tritium transport, three simplified models are developed, using a step-by-step approach, in order to understand the complex phenomena produced by the multiple coupled physics. A straight rectangular duct that contains zero, one and two coolant tubes and with an Eurofer baffle on top. They are presented in Fig. 4.10. In the case with two tubes, in the left one water flows in the opposite direction with respect to the PbLi, while in the right tube it flows in the same direction.

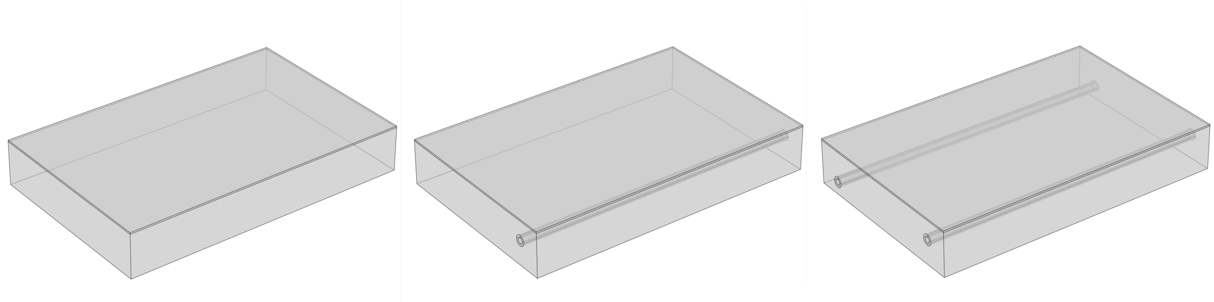

Figure 4.10: The three simplified models zero, one and two tubes.

Water is solved using the turbulent model $k - \omega$, while in the PbLi the flow is laminar. For what regards heat transfer, the contribution of the volumetric heat generation rate is included, and the boundary condition for tritium transport are explained in Section 2.2.

For the three geometry MHD and tritium transport for $Ha = 0, 50, 100$ and magnetoconvection and tritium transport for $Ha = 50$ are solved following the procedure expressed in Figure 2.6. The results are presented in the following sections.

4.2.1 MHD and tritium transport results

For the three simplified geometries, magnetohydrodynamics without buoyancy and tritium transport are solved.

Considering the zero tube case, in Fig. 4.11a the PbLi velocity profile in the z direction at the middle of the outlet section for different Ha numbers is shown . It is evident the M-shape profile for the MHD cases. In Figure 4.11b the velocity profile in the toroidal-poloidal plane at the outlet for $Ha = 50$ is shown . The tritium losses and inventories, defined by equations 2.113 and 2.114, are presented in Table. 4.2. The permeation rate, defined as the surface integral of the normal total flux on the interfaces between the PbLi and the Eurofer, can be seen in Fig. 4.12. It is interesting to see that it decrease as the Hartmann number increases, as reported also by Zhang [43].

The same results are also reported for the one tube and two tubes cases. It is interesting to see in Figure 4.13a and 4.15a that the M-shape profile is still present, but is deformed by the presence of the tubes. There is also the presence of velocity spikes near the tubes, parallel to the magnetic field direction (Fig. 4.13b and 4.15b). The permeation rate become bigger as the number of tubes increases, and this ultimately impact the losses. This is due to the increased interface area between the PbLi and the Eurofer.

The mass balance of tritium has been carried out to verify the accuracy of the results. The tritium generated at each time must be equal to the tritium permeated in the Eurofer domain, plus the tritium accumulated and the tritium that escape from the boundaries. The integral mass balance error is smaller than 10% for every case, with the exception of the one tube, $Ha = 100$ case (11.37%) and the two tubes, $Ha = 100$ case (11.06%).

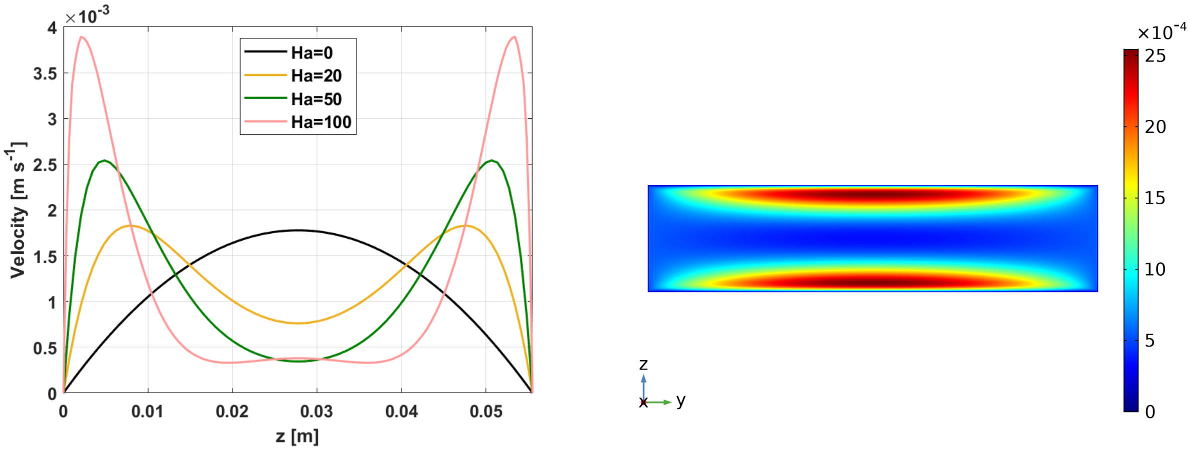

(a) Velocity on z-direction for different Ha.

(b) Velocity in a poloidal-toroidal plane.

Figure 4.11: Velocity profile at the outlet section for the MHD without buoyancy and zero tubes case.

	Losses [%]	Inventories [mol]			
Ha		PbLi	Water	Baffle	Pipes
0	1.2844×10^{-1}	3.8854×10^{-6}		5.3827×10^{-7}	
50	9.8332×10^{-2}	2.9383×10^{-6}		1.3991×10^{-7}	
100	9.0681×10^{-2}	3.2520×10^{-6}		1.0522×10^{-7}	

Table 4.2: Tritium losses and inventories for the MHD without buoyancy and zero tubes case.

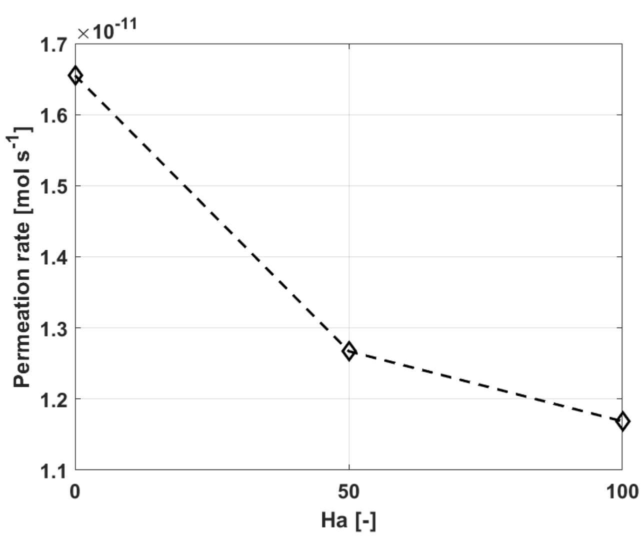

Figure 4.12: Permeation rate as function of the Hartmann number for the MHD without buoyancy and zero tubes case.

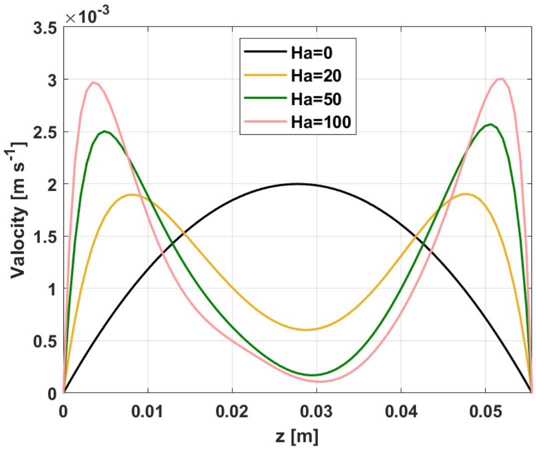

(a) Velocity on z-direction for different Ha.

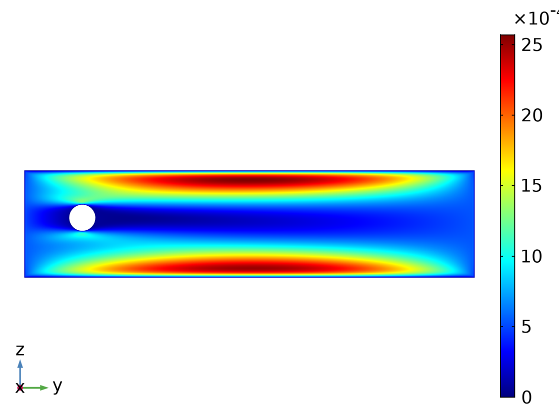

(b) Velocity in a poloidal-toroidal plane.

Figure 4.13: Velocity profile at the outlet section for the MHD without buoyancy and one tube case.

	Losses [%]	Inventories [mol]			
Ha		PbLi	Water	Baffle	Pipes
0	1.4968×10^{-1}	4.2464×10^{-6}	4.1943×10^{-11}	5.5190×10^{-7}	1.0053×10^{-7}
50	1.1445×10^{-2}	3.4970×10^{-6}	2.8523×10^{-11}	1.4045×10^{-7}	6.7775×10^{-8}
100	1.0661×10^{-1}	3.6811×10^{-6}	2.7345×10^{-11}	1.0614×10^{-7}	6.4872×10^{-8}

Table 4.3: Tritium losses and inventories for the MHD without buoyancy and one tube case.

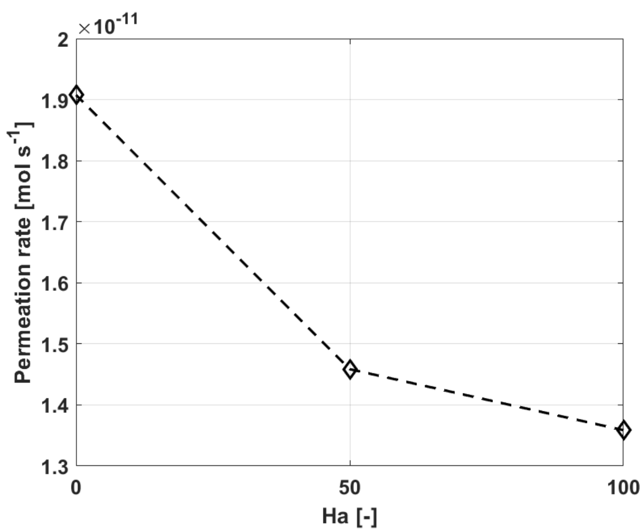

Figure 4.14: Permeation rate as function of the Hartmann number for the MHD without buoyancy and one tube case.

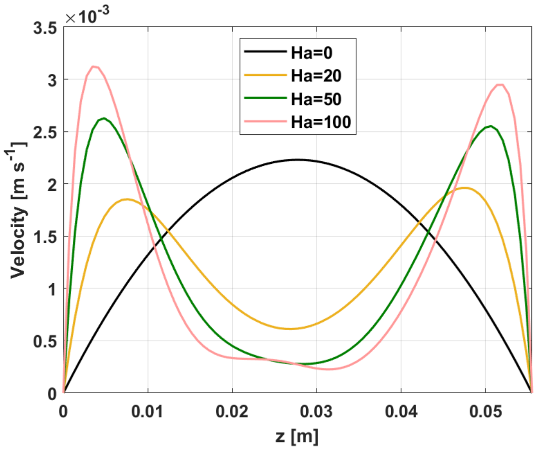

(a) Velocity on z-direction for different Ha.

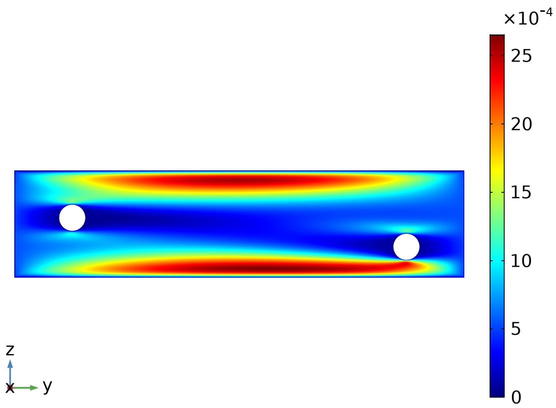

(b) Velocity in a poloidal-toroidal plane.

Figure 4.15: Velocity profile at the outlet section for the MHD without buoyancy and two tubes case.

	Losses [%]	Inventories [mol]			
Ha		PbLi	Water	Baffle	Pipes
0	1.6170×10^{-1}	4.5146×10^{-6}	6.2671×10^{-11}	5.3193×10^{-7}	2.0611×10^{-7}
50	1.2579×10^{-2}	3.4859×10^{-6}	4.1890×10^{-11}	1.4071×10^{-7}	1.2732×10^{-7}
100	1.1748×10^{-1}	3.6884×10^{-6}	4.0921×10^{-11}	1.0731×10^{-7}	1.2493×10^{-7}

Table 4.4: Tritium losses and inventories for the MHD without buoyancy and two tubes case.

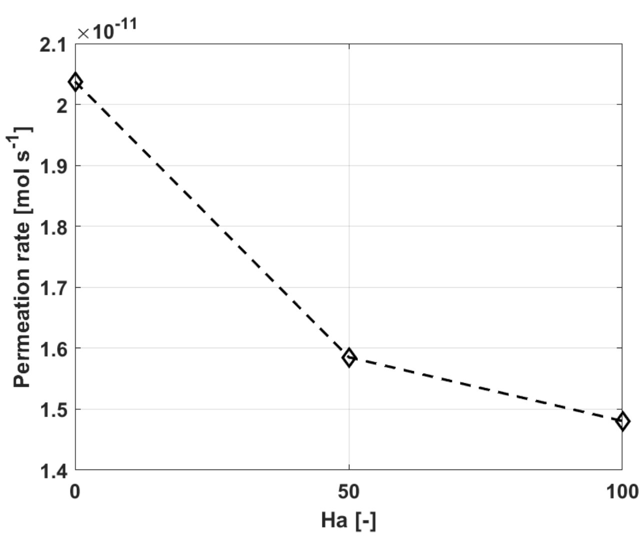

Figure 4.16: Permeation rate as function of the Hartmann number for the MHD without buoyancy and two tubes case.

4.2.2 Magnetoconvection and trititum transport results

The effect of buoyancy is now included in the study. The results are obtained for $Ha = 50$. As can be seen from Figures 4.17, 4.18 and 4.19, comparing the results to the pure MHD case, the velocity profile is completely changed by the effect of the gravitational term. Like in the CFD analysis (Section 4.1.2), in all the magnetoconvection cases, recirculation and backflow are present. From Table 4.5 is evident that for the magnetoconvection case permeation rates are increased and tritium inventories are smaller. The integral mass balance error is smaller than 10% for the zero and one tubes geometries, but is 20.94% for the two tubes case.

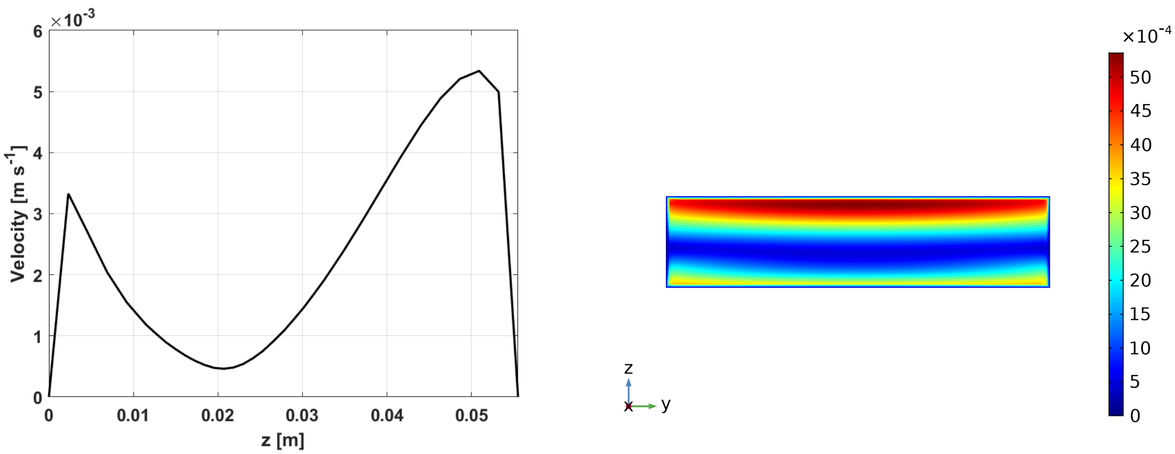

(a) Velocity on z-direction for different Ha. (b) Velocity in a poloidal-toroidal plane.

Figure 4.17: Velocity profile at the outlet section for the magnetoconvection and zero tubes case.

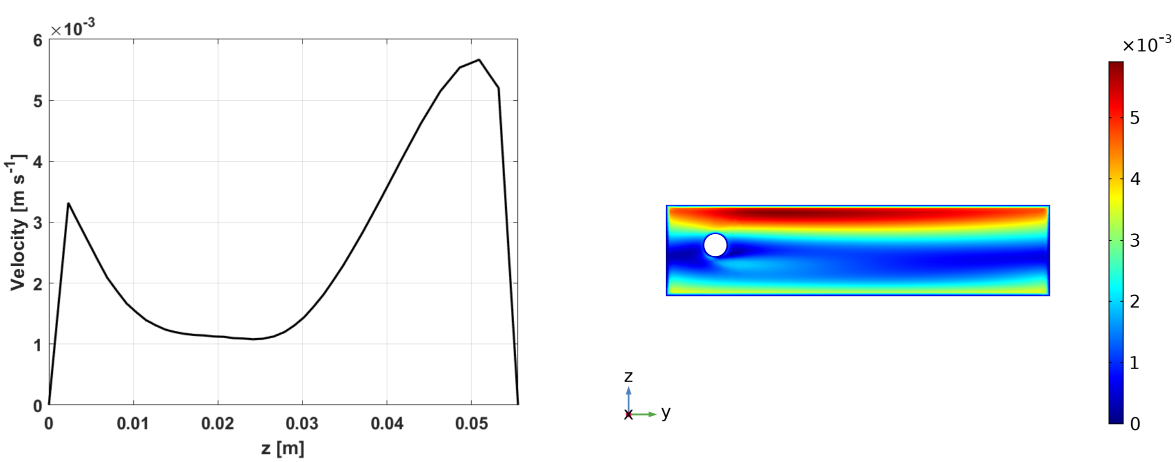

(a) Velocity on z-direction for different Ha. (b) Velocity in a poloidal-toroidal plane.

Figure 4.18: Velocity profile at the outlet section for the magnetoconvection and one tube case.

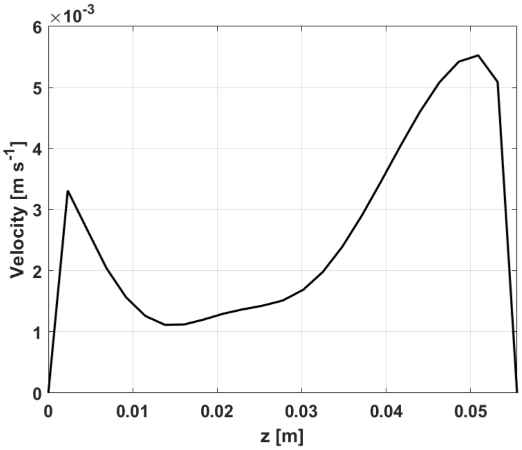

(a) Velocity on z-direction for different Ha.

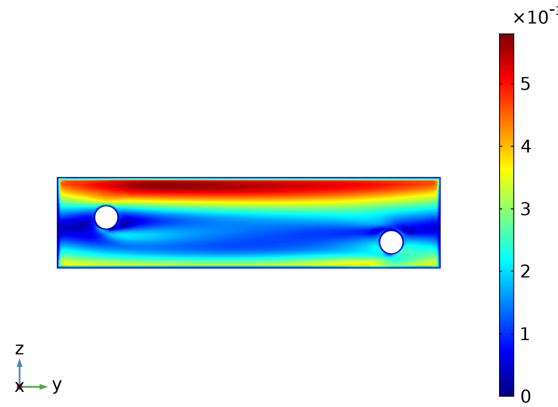

(b) Velocity in a poloidal-toroidal plane.

Figure 4.19: Velocity profile at the outlet section for the magnetoconvection and two tubes case.

	Losses [%]	Inventories [mol]			
Geometry		PbLi	Water	Baffle	Pipes
0T	1.8309×10^{-1}	1.6493×10^{-6}		7.6442×10^{-8}	
1T	2.4754×10^{-2}	1.7511×10^{-6}	4.2331×10^{-12}	6.9361×10^{-8}	8.2248×10^{-9}
2T	2.5402×10^{-1}	1.5398×10^{-6}	7.8346×10^{-12}	6.7336×10^{-8}	2.4240×10^{-8}

Table 4.5: Tritium losses and inventories for the magnetoconvection case.

Conclusions

In the work, the analysis of half the WCLL module has been carried out. An extensive benchmark activity to verify the reliability of the codes developed has been carried out. Three different flows are investigated, 2D fully developed MHD flow, 3D MHD flow in a non-uniform magnetic field and MHD with buoyancy. The solution of the CFD model has been obtained, comparing the case without buoyancy with the buoyancy case. The impact of buoyancy on the temperature and velocity field is considerable. Buoyancy mitigates and smoothen the temperature field, and the presence of temperature gradients creates eddys and recirculating patterns inside the module, causing backflow in the outlet section. This phenomenon must be further investigated.

The breeding unit has a complex geometry, and the introduction of additional physics, MHD and tritium transport, requires substantial computational resources. For this reason, the MHD effect has been analyzed considering three simplified geometries of the WCLL, a rectangular duct with zero, one and two coolant tubes. The pure MHD case was solved for different Hartmann numbers, and a decrease of the permeation rate with the increase of Ha is evident. The case without buoyancy forces is then compared to the buoyancy case. Magnetoconvection has again a large effect on the flow behavior, produces backflow, and tends to reduce the concentration of tritium in all the domains, and increases the losses.

The computational errors, evaluated performing a mass balance, are acceptable, but further investigation of the work is needed in order to reduce them as much as possible, particularly for the two tubes cases. Additional advances include the analysis of the simplified models considering higher Hartmann numbers, particularly the Ha representative for fusion applications ($Ha > 1000$), and the comparison of the results with different codes.

Bibliography

[1] R. Arnoux. Tritium: changing lead into gold. `https://www.iter.org/mag/8/56`, 2016.

[2] C. Bachmann et al. Initial DEMO tokamak design configuration studies. *Fusion Engineering and Design*, 98-99:1423–1426, 2015.

[3] G. K. Batchelor. On the spontaneous magnetic field in a conducting liquid in turbulent motion. *Proceedings of the Royal Society of London. Series A, Mathematical and Physical Sciences*, 201(1066):405–416, 1950.

[4] E. Blums, Y. Mikhailov, and R. Ozols. *Heat and mass transfer in MHD flows*. World Scientific, 1987.

[5] L. V. Boccaccini et al. Objectives and status of EUROfusion DEMO blanket studies. *Fusion Engineering and Design*, 109-111:1199–1206, 2016.

[6] V. Bojarevics. Buoyancy driven flow and its stability in a horizontal rectangular channel with an arbitrary oriented transversal magnetic field. *Magnetohydrodynamics*, 31(3):245–253, 1996.

[7] L. Buhler. Laminar buoyant magnetohydrodynamic flow in vertical rectangular ducts. *Physics of Fluids*, 10(223), 1998.

[8] L. Candido et al. Development of advanced hydrogen permeation sensors to measure Q2 concentration in lead-lithium eutectic alloy. *Fusion Engineering and Design*, 124:735–739, 2017.

[9] L. Candido et al. Tritium transport model at breeder unit level for WCLL breeding blanket. *Fusion Engineering and Design*, In press, 2019.

[10] M. Casey and T. Wintergerste. *Best practice guidelines*. ERCOFTAC, 2000.

[11] O. G. W. Cassels, T. Vo, A. Pothérat, and G. J. Sheard. From three-dimensional to quasi-two-dimensional: transient growth in magnetohydrodynamic duct flows. *Journal of Fluid Mechanics*, 861:382–406, 2019.

[12] I. Celik. Numerical uncertainty in fluid flow calculations: needs for future research. *ASME Journal of Fluid Engineering*, 115:194–195, 1993.

[13] P. A. Davidson. *An introduction to Magnetohydrodynamics*. Cambridge University Press, 2001.

[14] J. P. Garandet and T. Alboussiere. Buoyancy driven convection in a rectangular enclosure with a transverse magnetic field. *International Journal of Heat and Mass Transfer*, 35(4):741–748, 1992.

[15] J. Hartmann. Hg-dynamics I. *Mathematisk-fysiske meddelelser*, 15(6), 1937.

[16] J. C. R. Hunt. Magnetohydrodynamic flow in rectangular ducts. *Journal of Fluid Mechanics*, 21(4):577–590, 1965.

[17] M. Iacolino. Tritium transport model at breeder unit level for WCLL breading blanket. Master's thesis, Politecnico di Torino, 2018.

[18] T. Kajishima and K. Taira. *Computational fluid dynamics - Incompressible turbulent flows*. Springer, 2017.

[19] A. Kharicha, S. Molokov, S. Aleksandrova, and L. Buhler. Buoyant convection in the HCLL blanket in a strong, uniform magnetic field. 2004.

[20] P. L. Kirillov. *Thermophysical properties of materials for nuclear engineering*. IAEA, 2006.

[21] P. K. Kundu and I. M. Cohen. *Fluid mechanics*. Elsevier, 2008.

[22] N. Ma and J. S. Walker. Liquid-metal buoyant convection in a vertical cylinder with a strong vertical magnetic field and with a nonaxisymmetric temperature. *Physics of Fluids*, 7(2061), 1995.

[23] A. Del Nevo et al. Recent progress in developing a feasible and integrated conceptual design of the WCLL BB in EUROfusion project. *Fusion Engineering and Design*, In press, 2019.

[24] M. -J. Ni et al. A current density conservative scheme for incompressible MHD flows at low magnetic Reynolds number. Part II: On an arbitrary collocated mesh. *Journal of Computational Physics*, (227):205–228, 2007.

[25] P. Norajitra et al. *Conceptual design of the dual-coolant blanket in the frame for the EU power plant conceptual study (TW2-TRP-PPCS12D)*, 2002.

[26] I. Di Piazza and L. Buhler. Numerical simulations of buoyant magnetohydrodynamic flows using the CFX code. 1999.

[27] B. F. Picologlou and C. B. Reed. Experimental investigation of 3-D MHD flows at high harmann numbers and interaction parameters. 1988.

[28] C. B. Reed et al. Alex results: A comparison of measurements from a round and a rectangular duct with 3-D code predictions. 1987.

[29] C. B. Reed, B. F. Picologlou, and P. V. Dauzvardis. Experimental facility for studying MHD effects in liquid metal cooled blankets. *Fusion Technology*, 8:257–263, 1985.

[30] P. J. Roache et al. Editorial policy statement on the control of numerical accuracy. *ASME Journal of Fluid Engineering*, 108:2, 1986.

[31] F. Romanelli et al. *Fusion electricity - A roadmap to the realisation of fusion energy*, 2012.

[32] S. Sahu and R. Bhattacharyay. Validation of comsol code for analyzing liquid metal magnetohydrodynamic flow. *Fusion Engineering and Design*, 127:151–159, 1985.

[33] J. A. Shercliff. Steady motion of conducting fluids in pipes under transverse magnetic fields. *Mathematical Proceedings of the Cambridge Philosophical Society*, 49:136–144, 1953.

[34] S. Smolentsev et al. An approach to verification and validation of MHD codes for fusion applications. *Fusion Engineering and Design*, 100:65–72, 2015.

[35] S. Smolentsev, N. B. Morley, and M. A. Abdou. Code development for analysis of MHD pressure drop reduction in a liquid metal blanket using insulation technique based on a fully developed flow model. *Fusion Engineering and Design*, 73:83–93, 2005.

[36] J. Sommeria and R. Moreau. Why, how, and when, MHD turbulence becomes two-dimensional. *Journal of Fluid Mechanics*, 118:507–518, 1982.

[37] A. Sterl. Numerical simulation of liquid-metal MHD flows in rectangular ducts. *Journal of Fluid Mechanics*, 216:161–191, 1990.

[38] D. Stork. *DEMO and the route to fusion power*, 2009.

[39] R. Testoni et al. Tritium transport model at breeder unit level for HCLL breeding blanket. *Fusion Engineering and Design*, In press, 2019.

[40] M. Utili et al. Status of Pb-16Li technologies for european DEMO fusion reactor. *Fusion Engineering and Design*, In press, 2019.

[41] C. P. C. Wong et al. *Design description document for the U.S. dual coolant Pb-17Li (DCLL) test blanket module*, 2005.

[42] H. Zhang. *Modeling and analysis of tritium transport in multi-region Lead-Lithium liquid metal blankets*. PhD thesis, University of California, 2014.

[43] H. Zhang, A. Ying, and M. Abdou. Quantification of dominating factors in tritium permeation in PbLi blankets. *Fusion Science and Technology*, 68(2):362–367, 2015.